The Evolution of an Observed Cold Front. Part II: Mesoscale Dynamics

ISIDORO ORLANSKI AND BRUCE B. ROSS

Geophysical Fluid Dynamics Laboratory/NOAA, Princeton University, Princeton, NJ 08540

(Manuscript received 4 April 1983, in final form 27 February 1984)

ABSTRACT

A detailed analysis is made of a three-dimensional numerical simulation of the evolution of an observed moist frontal system over a 48 h period. The simulated front undergoes an initial period of frontogenetic growth, characterized by an alignment of vertical vorticity and horizontal convergence near the surface. The front then evolves to a mature, quasi-steady state as the line of maximum convergence moves ahead of the maximum vorticity. This phase shift is shown to be the result of a negative feedback mechanism which inhibits further vorticity growth while reducing the amount of viscous damping required to achieve a steady state. The influence of viscosity and surface drag upon this mechanism is also assessed.

When moisture is included in the numerical solution, the squall line which develops along the front exhibits a dual updraft structure with low-level convergence near the nose of the front and midlevel convergence located 100 km to the rear at a height of 3 km. This configuration is very similar to that found by Ogura and Liou in their analysis of an Oklahoma squall line not associated with a cold front.

Analysis of the equations of motion within the convective zone of the mature squall line shows the diabatic heating to be closely balanced by adiabatic cooling due to vertical temperature advection. As a result, the only net warming within this region occurs as adiabatic warming in the clear air outside of the cloud zone.

A linear, two-layer, dry model containing stable lower and unstable upper layers is shown to reproduce the dual updraft structure for certain low-level wind intensities without requiring microphysics. Also, for all wind conditions, this simple model produces strong convergence at the interface between the two layers. This suggests that the occurrence of a convergence maximum at the level of free convection should be a common feature of convectively unstable cloud systems.

1. Introduction

A simulation of the evolution of an observed cold front and its associated convection is described in an earlier companion paper (Ross and Orlanski, 1982, hereafter referred to as RO). In the present paper, a detailed analysis of this numerical solution is presented for the purpose of identifying the dynamical balance and the controlling forces which occur in a mature front.

A two-dimensional frontal simulation investigated by Orlanski and Ross (1977) produced a realistic, steady-state frontal system similar to those observed in nature. In this solution, the ageostrophic cross-stream circulation was shown to be an important feature of the steady-state front. Also, it was found that strong viscous damping was not needed to maintain the stationarity of the mature frontal system. On the other hand, solutions using semigeostrophic equations of motion (e.g., Hoskins and Bretherton, 1972; Hoskins and West, 1979) and primitive equations (Williams, 1967), have been shown to require dissipation to limit frontal intensification. In fact, Hoskins and Bretherton (1972) found good agreement between their frontal solutions using the semigeostrophic equations and the numerical solutions of Williams (1967) using the primitive equations. However, in Section 2a we will show that, although the similarity of both solutions is quite good during the initial development of frontogenesis, certain important features develop in Williams' solution during its later stages, which reflect the ageostrophic tendencies to be discussed in this paper. [McWilliams and Gent (1980) and Blumen (1980) have also pointed out that the semigeostrophic equations may fail to simulate certain features in frontal dynamics.]

In this paper, we will analyze the numerical simulation of an observed case of frontal evolution and squall-line development. The primary purpose of this analysis will be to better understand the role which ageostrophic, subsynoptic effects play in maintaining the frontal vertical cross-stream circulation, and to determine the influence which this circulation has in initiating and sustaining a line of deep convection above the surface front. In addition, the structure of this convection will be analyzed in detail and will be compared to the observed structure of another extratropical squall-line.

Section 2 contains an analysis of the ageostrophic dynamical balance which develops in the modeled surface front after an initial frontogenetic period. The significance of this ageostrophic feature is that it represents an alternate mechanism to viscous damping alone, by which the frontal system is able to curtail

the unbounded vorticity growth which quasi-geostrophic frontogenesis theories predict. In the third and succeeding sections, different features of the frontal convection in the numerical simulation are described and analyzed. Section 3 presents an analysis of the structure and dynamics of the moist convection, which is represented explicitly by the numerical model. Then, in Section 4 a linear dry, analytical model is formulated as a prototype of the unstable cloud environment. The structure of some of the unstable modes which develop in this simple model is very similar to that found in the present convection simulation and also in another observed squall line, thereby suggesting a possible cause of these convective features.

2. Dynamical balance at the surface

In the cold front system investigated here, the most intense frontal dynamics will obviously occur near the surface. As shown by Hoskins and West (1979), the evolution of such a system may thus be characterized by the dynamical balances which develop at the lower boundary. Furthermore, the vanishing of the vertical velocity w, together with the simplifying assumption of free slip at the surface where $z = 0$, permit us to greatly simplify the equations of motion at the surface, including the equations of horizontal divergence $\mathcal{D}$ and vertical relative vorticity ζ. Accordingly, in the present section we will analyze the cold front simulation described by RO in terms of the vorticity and divergence equations evaluated near the surface. Specifically, the simpler surface dynamics of the dry front stimulation will be studied in Section 2a, while the more complex behavior of the frontal system with moisture included will be considered in Section 2b. The vertical frontal structure of different terms in the equations of motion are described in the Appendix, and a brief discussion of important terms within the convective region is also given in Section 3d.

a. Dynamics of the dry front

In the simulation described by RO, a cold front was shown to intensify during an initial frontogenetic stage (due in part to the coarseness of the initial observed field) and then to decay near the end of the 48 h period. The intensification and weakening of the surface confluence along the front is clearly apparent in the surface streamline patterns displayed in Fig. 1 at 12 h intervals. At 6 h, the trough of the baroclinic wave, with the associated cyclonic flow C, is evident in the upper portion of the domain where streamlines enter from the northwest, sweep southeastward across the Great Plains, and then turn cyclonically to the northeast to exit the domain around the Great Lakes. The dominant northeastward flow is enhanced by an anticyclonic flow A_2 from the Gulf of Mexico, which is driven by a high pressure system to the east of the domain. In addition, an anticyclonic pattern A_1 near the northwest boundary indicates the presence of a high pressure system northwest of the domain. This configuration of high–low–high is typical of a developing baroclinic wave.

As is often the case (Hoskins, 1976; Mechoso, 1980), the further evolution of the baroclinic wave shows a tendency for the low-pressure center (located north of Iowa at 6 h) to move poleward while the adjacent high pressure centers move equatorward. As a result, the anticyclones A_1 and A_2 tend to move closer together, as occurs at 18 h in Fig. 1. The cyclonic flow is then squeezed between these two highs, thereby causing frontogenesis as the line of vorticity which separates the cyclonic and anticyclonic flows is increased due to local convergence and the accompanying vortex stretching.

Air parcels passing between A_1 and C at 18 h may go either south and then west, following the western anticyclonic flow A_1, or else southeast and then northeast, following the eastern cyclonic flow C. A large amount of cyclonic vorticity is generated in the latter trajectory. This vorticity is enhanced further at 30 h, as shown in the figure by the narrow band of strong cyclonic curvature over the southeastern states. The intensity of the dry cold front is maximum at this time. Finally, at 42 h the cold front is in a period of decay. From a synoptic viewpoint, the two anticyclonic flows A_1 and A_2 appear to be merging at this time while the region of cyclonic flow C has moved well to the north.

The evolution of the synoptic systems described above may also be characterized in terms of the energy transfer which occurs between different wavenumbers in an evolving baroclinic wave. The energy source for this wave is the potential energy of the zonal flow which is transferred by baroclinic instability to modify the mean flow. As the wave matures, part of its energy is lost through a cascade to higher wavenumbers; this transfer of energy may be viewed as causing frontogenesis (Andrews and Hoskins, 1978). At the same time, however, there is also a decascade of energy to lower wavenumbers. In fact, in its final stage, the merging of the anticyclones in the wave, which is apparent in Fig. 1 at 42 h, can be viewed as evidence of this decascade, which was suggested in the theory of quasi-geostrophic turbulence (Charney, 1971).

The most important features of the surface winds are apparent from an inspection of the fields of vertical relative vorticity and horizontal convergence as shown in Fig. 2 at 6 h intervals during the frontal evolution. (Hereafter, the term "vorticity" as used in the text will be assumed to refer to the vertical relative vorticity component $v_x - u_y$ unless stated otherwise.) The narrow zone of intense vorticity indicates the location of the surface cold front for each time in the sequence. Note, in particular, that the convergence band is displaced to the warm air side of the vorticity band so that the two bands are nearly out of phase with each other because the maximum convergence is close to the line of zero vorticity. As will be discussed below, this configuration is particularly significant because,

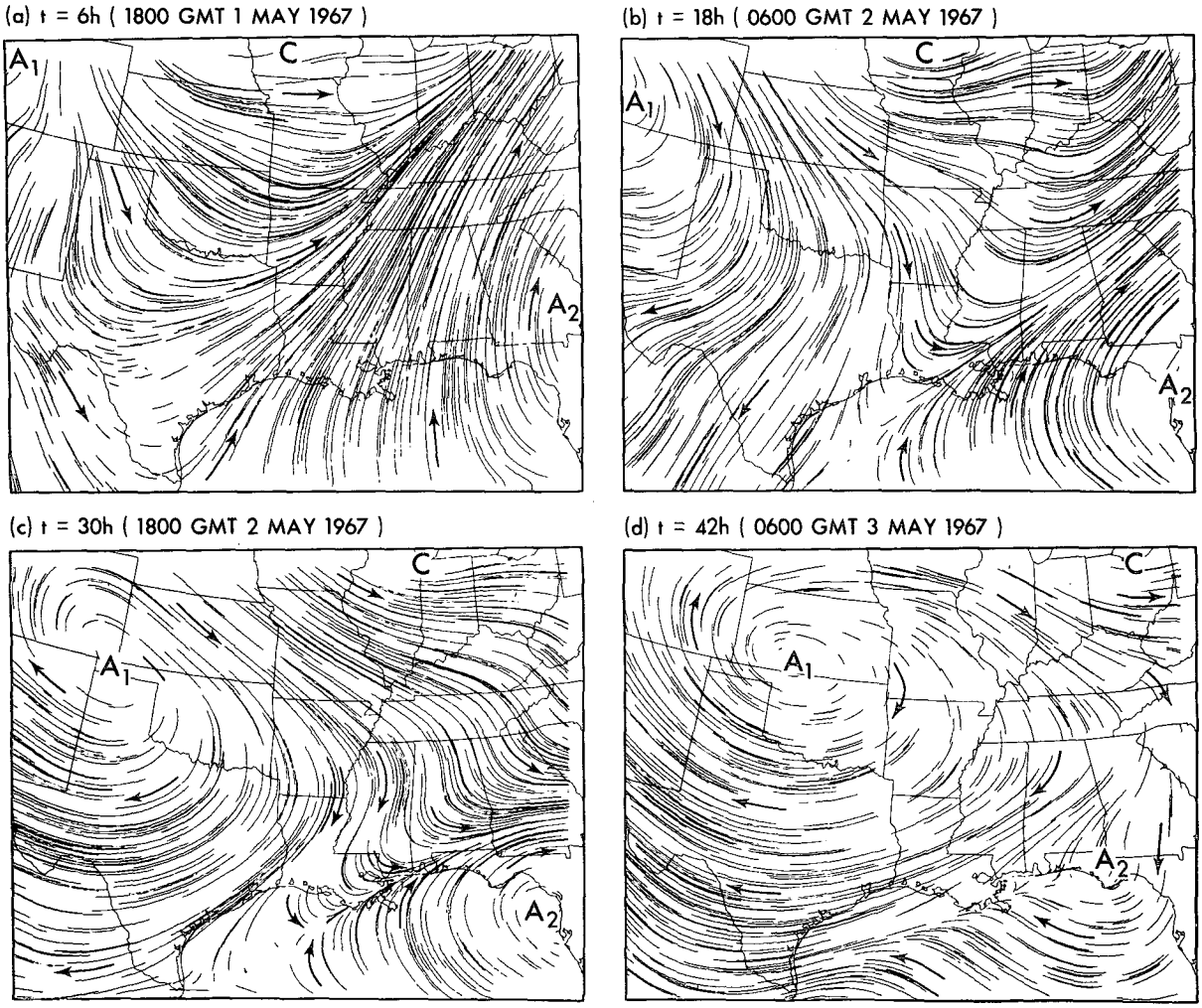

FIG. 1. Maps of surface streamlines from the dry solution at four different times. Letters A and C indicate regions of anticyclonic and cyclonic flow, respectively, as discussed in the text.

in a frontogenetic process, horizontal convergence must be in phase with vorticity if stretching is to produce maximum vorticity intensification. The fact that this phase shift exists in the numerical simulation of the mature frontal stage shown in Figs. 2b and c, suggests that a feedback mechanism has developed during the frontal evolution to reduce the earlier frontogenetic growth.

It is instructive to display the evolution (Fig. 3) of surface vorticity and divergence in the dry solution along the line MN shown in the 36 h frame of Fig. 2. During the early stages of the period, the observed front indicated some frontogenetic development. However, because the model simulation was initialized from observed data which were gridded to a 246 km resolution grid, an artificially intense frontogenesis occurs in the numerical solution during the first 6–12 h of the simulation as the meso-α scale frontal vorticity intensifies. The frontogenetic nature of the system is clearly evident at 6 h in Fig. 3, with in-phase alignment of vorticity and convergence. By 12 h, vertical vorticity has nearly doubled in magnitude due to vortex stretching, while the convergence maximum has weakened and shifted well ahead of the vorticity maximum. Both fields still exhibit the meso-α horizontal scales of the initial front.

During the ensuing period from 12 to 30 h, the width of the positive vorticity band along cross-section MN decreases from 480 to 190 km. (The actual width of the band at 12 h appears to be 550 km in Fig. 3 because the front intersects MN at an angle of 30° from the perpendicular at this time. During the period from 24 to 48 h, the correction needed for this geometric effect is less than 5%.) For the remainder of the solution this width is constant at 190 km. Throughout this period in which the frontal scale decreases, the maximum value of the vorticity along MN remains roughly constant, while Fig. 2 indicates that the maximum within the entire frontal band increases slightly between 24 and 30 h.

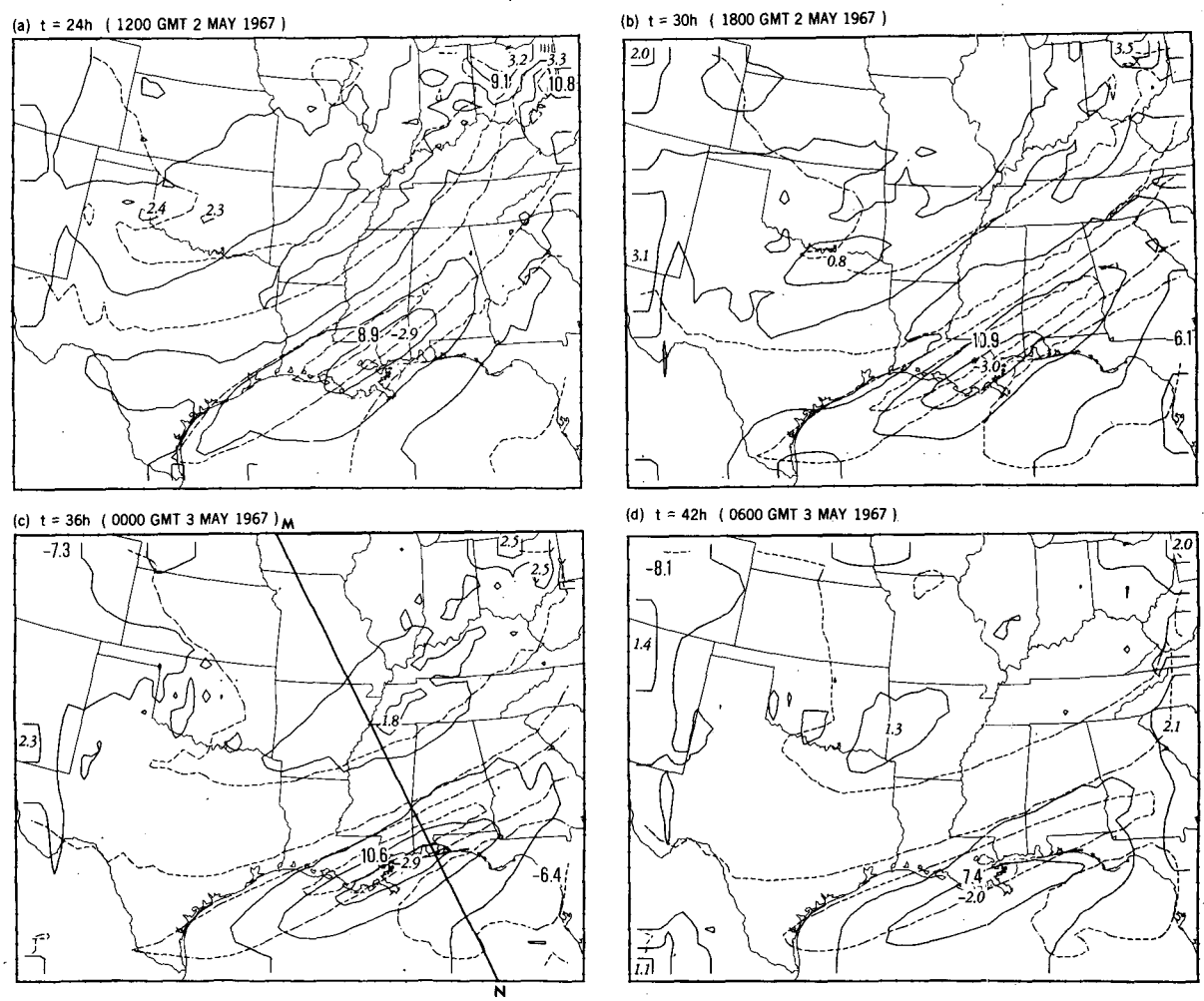

FIG. 2. Composite maps of horizontal divergence $\mathcal{D}$ (solid contours with extrema indicated in italics) and vertical vorticity ζ (dashed contours with extrema indicated in standard numerals) at the surface in the dry solution at four different times. Divergence and vorticity values are shown in units of 10^{-5} s^{-1}. Contour intervals are $\Delta\zeta = 5 \times 10^{-5}$ s^{-1} and $\Delta\mathcal{D} = 1 \times 10^{-5}$ s^{-1}. The line segment MN indicates the orientation of the axis of the plots shown in Figs. 3, 4 and 9.

The behavior of the convergence field is more oscillatory than is vorticity, although an obvious trend toward decreasing horizontal scale is evident from 12 to 36 h. The extreme shift in the convergence maximum at 12 h to a position 400 km ahead of the vorticity maximum is followed by a much less pronounced shift for the following times.

Although the width of the vorticity band remains constant along MN over the last day of the simulation, an obvious frontolysis is apparent in Fig. 3 at 42 and 48 h, which was shown by Fig. 2 to occur over the entire dry front. During this period, both the vorticity and convergence magnitudes are reduced to nearly half their earlier values while the widths of the convergence as well as the vorticity bands are unchanged.

We will show in the following discussion that ageostrophic effects produce frontolytic processes when the frontal vorticity becomes sufficiently intense. These processes act to limit further intensification of the front by displacing the convergence maximum so that it is more out of phase with the vorticity maximum and thus is unable to maintain its original level of vortex stretching. In order to better understand the way in which such a feedback mechanism will act, we consider now the equations for vertical vorticity ζ and horizontal divergence $\mathcal{D}$ as defined at the surface $z = 0$. These equations may be derived from (2.1) of RO to give

$$\frac{D\zeta}{Dt} = -(f + \zeta)\mathcal{D} + F_\zeta, \tag{2.1}$$

$$\frac{D\mathcal{D}}{Dt} = (f + \zeta)\zeta - c_p\theta_0\nabla^2\pi - \frac{1}{2}[\nabla^2(\mathbf{V}\cdot\mathbf{V}) - 2\mathbf{V}\cdot\nabla^2\mathbf{V}] + F_{\mathcal{D}}, \tag{2.2}$$

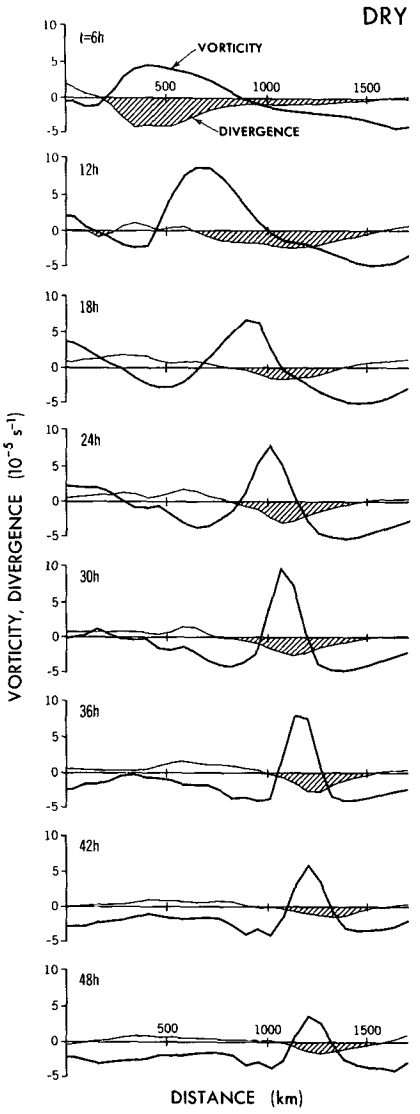

FIG. 3. Time variation of the distribution of vertical vorticity (heavy line) and horizontal divergence (light line) at the surface in the dry solution along the line MN shown in Fig. 2. Convergence is indicated by cross-hatching. The distance shown is measured along the line MN with the origin at the northern point M.

where D/Dt is the substantial derivative $(\partial/\partial t) + \mathbf{V}\cdot\nabla$ along the surface where $z = 0$, and F_ζ and $F_\mathcal{D}$ are turbulent diffusion terms. Note that the vanishing of w at $z = 0$ has eliminated terms for vertical advection and vorticity twisting from these equations.

Use of the quasi-geostrophic approximation would reduce Eqs. (2.1) and (2.2) to

$$\frac{D\zeta_g}{Dt} = -f\mathcal{D}_g + F_\zeta, \tag{2.3}$$

$$0 = f\zeta_g - c_p\theta_0\nabla^2\pi. \tag{2.4}$$

The approximate equation (2.4) is the same in both the quasi-geostrophic and the semi-geostrophic approximations and is the relevant expression upon which the following discussion will concentrate. Because the divergence equation (2.2) reduces to (2.4), the horizontal divergence $\mathcal{D}_g$ in this approximation must be obtained from the potential temperature equation as

$$\mathcal{D}_g = \frac{1}{\Gamma}\frac{D}{Dt}\left(\frac{\partial\theta}{\partial z}\right), \tag{2.5}$$

where Γ is the vertical potential temperature gradient of the undisturbed atmosphere. If the quasi-geostrophic equations (2.3)–(2.5) are to describe surface frontogenetic processes in which vorticity is intensified by vortex stretching (Williams and Plotkin, 1968; Hoskins and Bretherton, 1972), then the horizontal divergence $\mathcal{D}_g$ should be roughly in phase with the vorticity ζ_g. Consequently, the only mechanisms which are available in this equation system to prevent unbounded vorticity growth, assuming constant large-scale forcing, are 1) vorticity damping and 2) reduction of the frontal convergence by Eq. (2.5) through an alteration of the potential temperature field. Numerical studies (Williams, 1974; Hoskins and West, 1979) rely upon the former mechanism of viscous damping to prevent unlimited vorticity growth. It thus appears that the quasi-geostrophic representation of divergence by (2.5) does not provide an effective mechanism for displacing convergence from its initial position in phase with vorticity.

In order to identify possible negative feedback mechanisms which will tend to inhibit unbounded vorticity growth, we will now return to the full ageostrophic surface equations (2.1) and (2.2). The divergence equation (2.2) may be written as

$$\frac{D\mathcal{D}}{Dt} = f\zeta - c_p\theta_0\nabla^2\pi - [u_x^2 + 2v_xu_y + v_y^2] + F_\mathcal{D}, \tag{2.6}$$

where the vector expression in brackets in (2.2) has been expanded and combined with the term ζ^2. As the quasi-geostrophic equation (2.4) indicates, the primary geostrophic balance in (2.6) will be between the first two terms on the right-hand side of the equal sign. However, as vorticity increases relative to the pressure term during frontogenesis, a positive ageostrophic contribution to the divergence tendency will result in (2.6), thereby causing a reduction in the vertical lifting within the front. Other nonviscous terms on the right-hand side are quadratic and thus are of higher order than this effect. Hence the ageostrophic difference between the first two terms on the right-hand side of (2.6), which may be denoted as $f(\zeta - \zeta_g)$, represents the negative feedback mechanism to limit growth due to vortex stretching.

The use of the full divergence equation (2.6), rather than the quasi-geostrophic form (2.4), in the present case does not contradict the scale analysis given by

Hoskins and Bretherton (1972) which suggests that the semi-geostrophic approximation will be valid when

$$\frac{\zeta + f}{f} \ll \left(\frac{f}{D_g}\right)^2. \tag{2.7}$$

Here D_g is the horizontal geostrophic velocity deformation where the total horizontal deformation D is defined as

$$D = [(v_x + u_y)^2 + (u_x - v_y)^2]^{1/2}.$$

Calculation of the initial geostrophic deformation within the baroclinic zone in which the front will develop in the present solution shows values of D_g in the range 3×10^{-5} to 5×10^{-5} s^{-1}. Since the vorticity field is small compared to the Coriolis parameter f (0.8×10^{-4} s^{-1}), the initial ratio of the left-hand to the right-hand sides of (2.7) is around 1:5, indicating the semi-geostrophic approximation to be valid at this time, as one would expect. However, as the front intensifies, both D and D_g increase within the frontal zone (to the order of 10^{-4} s^{-1}), while the vorticity grows to be the order of f. As a result, the left-hand side of (2.7) is at least the order of the right-hand side during the period when the front is most intense (12–36 h). The lack of validity of (2.7) during this period justifies our use of the full divergence equation (2.6) rather than the approximate quasi-geostrophic equation (2.4).

Returning to (2.6), we note that divergence tendency will be maximum where the ageostrophic vorticity component is maximum if all other terms on the right-hand side of (2.6) may be neglected. Then if the convergence region within the front is initially in phase with the vorticity, the negative feedback will be maximum at the peak of convergence, thereby reducing the convergence field and hence the growth of vorticity due to stretching. These effects would then lead to an equilibrium in which the vorticity tendency is reduced to zero, with the remaining vortex stretching caused by the shifted convergence field being balanced by moderate dissipation. If dissipation is absent, an approximate equilibrium condition can only occur in a mature front when vorticity and convergence at the surface are out of phase (as in a neutral wave) with effectively no overlap. On the other hand, when dissipation is present in the solution, more overlap of vorticity and convergence can occur because the frontogenetic effects of vortex stretching at the surface can be balanced by the frontolytic influence of dissipation. Hence it might be expected that the phase shift between vorticity and divergence will decrease in a steady-state front as dissipative effects increase. Accordingly, simulations with large dissipative effects could achieve a steady-state front with virtually no phase shift. Also, it should be recognized that the present solution is quite idealized because of the free-slip condition used at the surface; as a result, the effects of surface friction will be absent from the dynamics of the surface front. It remains an open question as to how much atmospheric fronts in nature are controlled by dissipation, compared with the ageostrophic feedback mechanism introduced here. A simple sensitivity test will be presented at the end of this section to suggest the possible influence of dissipation and surface drag upon the vorticity and divergence distribution.

We have identified the ageostrophic vorticity term $f(\zeta - \zeta_g)$ as the primary mechanism suppressing vorticity growth. Let us now consider other terms in (2.1) and (2.6) for their influence upon vorticity growth at the surface. These terms can be more readily identified if we consider a purely two-dimensional front in which y-derivatives are neglected. In such a case, u_x represents the total divergence $\mathcal{D}$ and v_x the total vertical component of vorticity. The only nonzero term within the brackets on the right-hand side of the three-dimensional version of (2.6) is $-u_x^2$, which will produce negative divergence tendency and thus will tend to enhance convergence.

Weak three-dimensional effects such as frontal curvature will excite the other two terms within the brackets of (2.6), with $v_x u_y$ being the dominant term. Typical curvatures of a cold front (concave toward the cold air side) will produce negative u_y so that the term $v_x u_y$ will contribute positive divergence tendency in (2.6) (because vorticity, and hence v_x, is positive within the front). Thus if the front is completely two-dimensional, the system will be highly unstable because of the strong positive feedback caused by convergence in the full ageostrophic system. (The more unstable behavior of the two-dimensional front compared to three-dimensional configurations may explain why mesoscale systems such as rainbands have a tendency to occur as two-dimensional lines without need for direct forcing such as frontal lifting.)

An analysis has been made of the distribution and time variation of the terms in the vorticity and divergence equations as obtained from the dry frontal solution near the surface along the line MN of Fig. 2. Unfortunately, an exact correspondence between nonlinear terms in this analysis and the terms in (2.1) and (2.6) is not possible because of differences between the numerical representation of the equations and the form of the equations discussed above. However, we can draw some general conclusions. During the early part of the solution (corresponding to 6 h in Fig. 3), the Coriolis term $f\mathcal{D}$ dominates the right-hand side of (2.1), producing large positive vorticity tendency. At the same time, adjustment of the initial fields to a geostrophic balance is still incomplete, resulting in a large tendency for increased convergence ahead of the vorticity maximum. After this initial frontogenetic period, the tendencies of both vorticity and divergence become relatively small, with geostrophic balance predominating in (2.6). In fact, during this period (2.1) and (2.6) act as a coupled system of equations.

A simple analog form of (2.1) and (2.6) has been developed to model the interactions between these two equations at the surface. Integrations in time of these coupled ordinary differential equations show that vorticity and divergence within the surface front will oscillate about an equilibrium state with a frequency close to the inertial frequency which would apply for the limiting linear system. Indications of this oscillatory behavior are also evident in the analysis of terms discussed in the previous paragraph. However, such indications are only suggestive since the frontal solution decays after only two inertial periods.

When the front achieves an approximate steady state, some overlap may remain between the convergence and cyclonic vorticity within the front so that the remaining vortex stretching must be balanced by viscous dissipation. In the vorticity equation, this quasi-steady condition is indicated by a balance between the Coriolis term $f\mathcal{D}$, nonlinear forcing (primarily the stretching term $\zeta\mathcal{D}$), and viscous dissipation. In the divergence equation, geostrophic balance predominates but with the ageostrophic residue balanced by nonlinear forcing terms. Dissipation effects in the divergence equation are shown to be quite weak.

The simulation of two-dimensional frontogenesis in a baroclinic wave using a primitive-equation model (Williams, 1967) was shown by Hoskins and Bretherton (1972) to exhibit similar behavior to their semi-geostrophic frontogenesis solution. However, closer inspection of Williams' solution shows that the ageostrophic negative feedback mechanism discussed here also may occur in his solution in that the location of the maximum x-velocity component u (i.e., where $u_x = 0$) is aligned with the location of maximum v_x (see his Fig. 3 at $t = 5.5$ days). Thus, zero divergence ($u_x = 0$) occurs where vorticity v_x is maximum. The fact that Williams' front does not reach a steady state may be due to the unlimited potential energy source (constant $\partial\theta/\partial y$) which causes the continual growth of the baroclinic wave in his solution.

In view of the importance placed on dissipation as a mechanism to curtail vorticity growth in semigeostrophic frontogenesis studies, it is useful to determine the effect of different treatments of viscosity and surface drag at the surface in the present dry front solution. The solution described above, which will be referred to here as the *control,* uses simple, idealized surface conditions. *Free slip* is assumed at the surface, while the increased mixing which occurs in the planetary boundary layer is represented by a constant vertical viscosity of 20 $m^2\ s^{-1}$ at and below the 500 m grid level, and 10 $m^2\ s^{-1}$ at the 1500 m grid level. (As described in RO, nonlinear viscosity is used above these levels with a background value of 5 $m^2\ s^{-1}$ applied where Richardson number is large and positive.) Two other solutions will be compared with the control. In the first, a bulk drag parameterization is used to impose a *surface stress,* with a drag coefficient C_D of 0.00025. (The smallness of this coefficient compared to that typically used by other modelers is due to the 500 m height of the wind level used in this simplified drag treatment.) In this case, the vertical viscosity near the surface is the same as in the control. In the second case, the *free-slip surface condition* is retained, but the *vertical viscosity* in the levels at and below 1500 m is *reduced* to a constant value of 5 $m^2\ s^{-1}$ in order to match the background value in the free atmosphere above.

In all three solutions, three stages may be identified in the evolution of the front. Frontogenesis occurs during the initial period as the vorticity intensifies. A mature, quasi-steady period follows during which the vorticity is roughly out of phase with the divergence, and the vorticity is constant. Then a frontolytic period follows in which the vorticity and divergence amplitudes decay. In terms of the constancy of the vorticity maximum, the mature stages occur between 30 and 36 h in all three cases.

Figure 4 shows a comparison of the distribution of vorticity and divergence along the line MN (Fig. 2) for the three cases at the time when the front is mature. In the case with surface drag, the vorticity maximum is reduced to 90% of the control value while the divergence is effectively unchanged. When the surface viscosity is reduced but the free-slip condition is used, the vorticity maximum increases to 150% of the control value, while the divergence field is broader and slightly more intense. At first glance, it appears that viscosity alone is controlling the amplitude of the vorticity. However, at 30 h the divergence immediately below the vorticity maximum is reduced somewhat, suggesting a possible influence of the feedback mechanism due to the ageostrophic effect. As previously discussed, it is expected that, as the viscosity is reduced further, the equilibrium vorticity will increase but also with an accompanying enhanced ageostrophic feedback, so that the zero divergence line will move forward to be more aligned with the line of maximum vorticity. Note that, in all three cases, the convergence maximum is within one grid increment (61.5 km) of the zero vorticity at 30 h and is effectively aligned with the zero vorticity at 36 h. Hence the effective phase shift of the convergence field ahead of vorticity shows little sensitivity to the different surface dissipation conditions used here. The increased temporal variability shown in the convergence field in the low viscosity case is probably due to the increased effect of the nonlinear forcing terms in the divergence equation, as well as the presence of noise which is less damped by the lower viscosity.

The primary result of the above sensitivity tests is to demonstrate that the only dynamical effect upon the frontal solution of the changes in surface dissipation is to alter the magnitude of the cyclonic vorticity in the steady-state front. As will be discussed in Section 5, the cross-front temperature gradient increases in

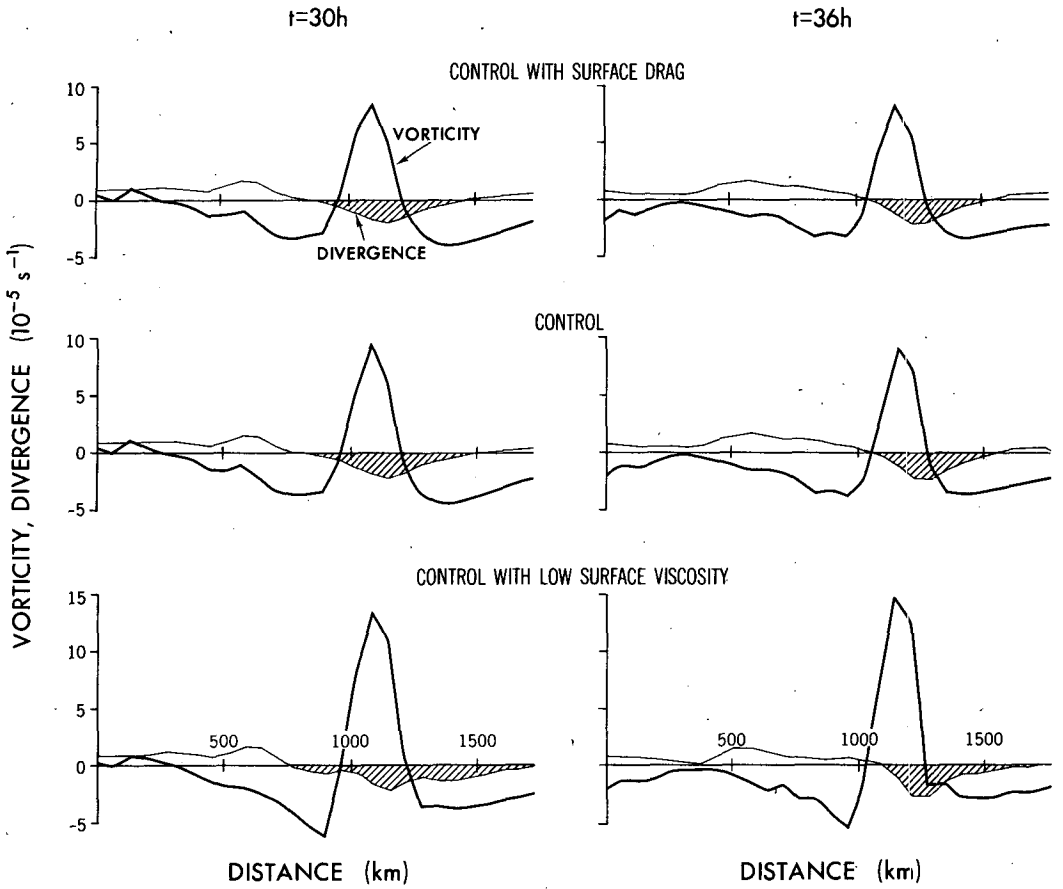

FIG. 4. Comparison of vertical vorticity and horizontal divergence along line MN (Fig. 2) for case with surface drag coefficient C_D = 0.00025 (top), control solution (middle) and case with low surface viscosity (bottom). Times are 30 and 36 h. Graphical display as in Fig. 3.

direct response to the thermal wind when vertical viscosity is reduced near the surface. However, Fig. 4 shows clearly that the width of the cyclonic vorticity band is unaffected by changes in the dissipation conditions. Finally, the low-level jet found by Keyser and Anthes (1982) when they included a planetary boundary layer in their two-dimensional idealized front was not observed in the present solution when surface drag was included. However, its absence may be due to the use of the simple bulk aerodynamic drag condition in the present case.

b. Moist front dynamics

The basic features of the moist front solution have been described in RO. In this subsection, we will emphasize the modifications which the presence of moisture produces in the structure of the front.

The large meso-α features of the baroclinic wave with moisture are quite similar to their counterparts in the dry case as was shown in RO. However, as might be expected, the organized moist convection which develops along the cold front alters the meso-β structure of the front considerably. For example, the intensified surface convergence at the front changes the surface streamline pattern shown in Fig. 1 at 30 h to the pattern shown in Fig. 5. The streamline convergence is much more intense in the frontal zone in the latter figure, while the flow field away from this region is virtually

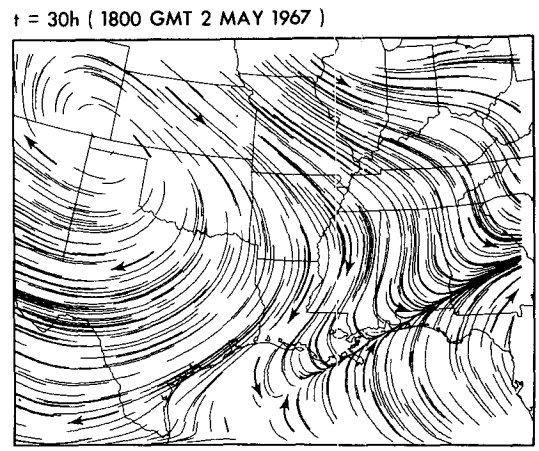

FIG. 5. As in Fig. 1, but from the moist solution.

unchanged. Note also in Fig. 5 that the cyclonic vorticity to the rear of the convergence line is more intense than that shown in Fig. 1. In fact, this streamline representation of surface flow patterns is another manifestation of the point made in Section 2a that the maximum convergence line tends to occur ahead of the maximum vorticity line in a mature front. This point will be discussed further in Section 5.

The moist equivalent of Fig. 2 for surface vorticity and convergence is shown in Fig. 6, where vorticity and divergence are plotted separately for successive six-hour time intervals with isobars of surface pressure included in each frame for reference. The times chosen for this figure represent the most active period of convection. Prior to 24 h in the simulation, the moist and dry solutions are quite similar.

A major change at 30 h in the vorticity and divergence patterns is evident from the fields in the dry solution. At this time, unstable convection along the convergence line is developing, with a nearly eightfold increase in the convergence along the front over its dry solution values (Fig. 2). This lifting then causes vorticity to more than double due to the stretching effect of the convection. In addition, the divergence and, to a lesser extent, the vorticity seem to be developing a cellular structure. Clearly one cause of this breakup of the vorticity and divergence lines is the tendency of the moist convection to form individual cloud elements. However, the fact that the vorticity band remains quite smooth until vorticity attains large values suggests that a barotropic instability due to the horizontal shear may also be important in producing the breakup in vorticity which is evident at 36 and 42 h in Fig. 6. Moore (1983) has shown that such a strong vorticity line will become barotropically unstable, with the most unstable wavelength along the line being equal to the thickness of the vorticity band. In the classical theory of barotropic instability, the aspect ratio between the depth and width of a shear zone must be much greater than 1 for the first internal mode to be unstable. This result would appear to indicate that convection associated with frontal rainbands is barotropically stable since the aspect ratio of such convective systems is close to or smaller than unity. However, Moore's stability analysis suggests that, when unstable stratification is included in a region of horizontal shear as might occur in a front, barotropic instability is possible when the depth of the region is less than or equal to its width. The barotropically unstable waves, which initially develop at the surface, will penetrate into the upper levels to produce cells over the whole depth of the convective zone (see Moore, 1983, for further discussion of this conditional instability). The cellular structure of the vertical velocity within the cloud zone in the upper levels at 36 h is shown in Fig. 7. Clearly the cell spacing is on the order of the thickness of the frontal vorticity band and, in the present solutions, is also limited by the model grid spacing of 61.5 km. In nature, this instability should occur on a smaller scale.

Radar observations (Hobbs, 1978; James and Browning, 1979) indicate that an organized cellular cloud structure often occurs within cold frontal rainbands. Hobbs and Biswas (1979) describe this structure in detail (their Fig. 1 is reproduced as Fig. 8 here). Although they do not give the cause of this pattern, Hobbs and Biswas find no evidence that vertical wind shear is involved. However, strong horizontal wind shear was observed for all cases in which the cells developed (P. V. Hobbs, personal communication, 1982). Although scale differences and lack of model resolution exist, the cells shown in Fig. 6 (see the divergence frame for 36 h) show an alignment with the axis of maximum convergence which is similar to that observed by Hobbs and Biswas.

The distribution of surface vorticity and divergence in the moist solution along the line segment MN (see vorticity at 36 h in Fig. 6) is shown in Fig. 9 at 6 h intervals from 18 to 48 h. Comparison of these curves with the analogous curves in the dry front case (Fig. 3) has indicated no significant differences for the period prior to 18 h. At 18 h, the only important change from the dry front curves is the convergence spike at 1100 km which indicates the initial development of the moist convection along the front. At 24 h, the convection-induced convergence is shown to dominate the dry-front convergence (Fig. 3). Both the vorticity and convergence maxima nearly double along this cross-section as compared to their dry solution counterparts.

During the ensuing period of the solution, the narrower convergence induced by the convection appears to dominate over the broader, weaker convergence pattern shown in the dry solution. The vorticity is also more intense than in the dry case due to vortex stretching, although the narrowing influence of the moisture is less pronounced because the band of cyclonic vorticity in the dry case was already quite narrow. During the last 24 h of the solution, when the moist convection is active, a phase shift of 60–120 km (1–$2\Delta x$) is still evident between the locations of maximum vorticity and convergence.

Throughout the mature period of the moist front, convergence is relatively small (near the changeover from negative to positive divergence) at the position in the front where vorticity is maximum. Thus, the discussion of phase shift in Section 2a still appears to be valid in the moist case. In fact, it appears that, in the moist convective system, the decrease in pressure close to the surface front due to latent heat release increases the convergence tendency [since $\nabla^2\pi$ is positive in (2.6)], while at the same time the vorticity intensification decreases convergence in a way analogous to that of the dry case.

As in the dry solution, a decay phase is apparent in the moist solution at 42 and 48 h, which is also evident from the increased disorganization of the surface con-

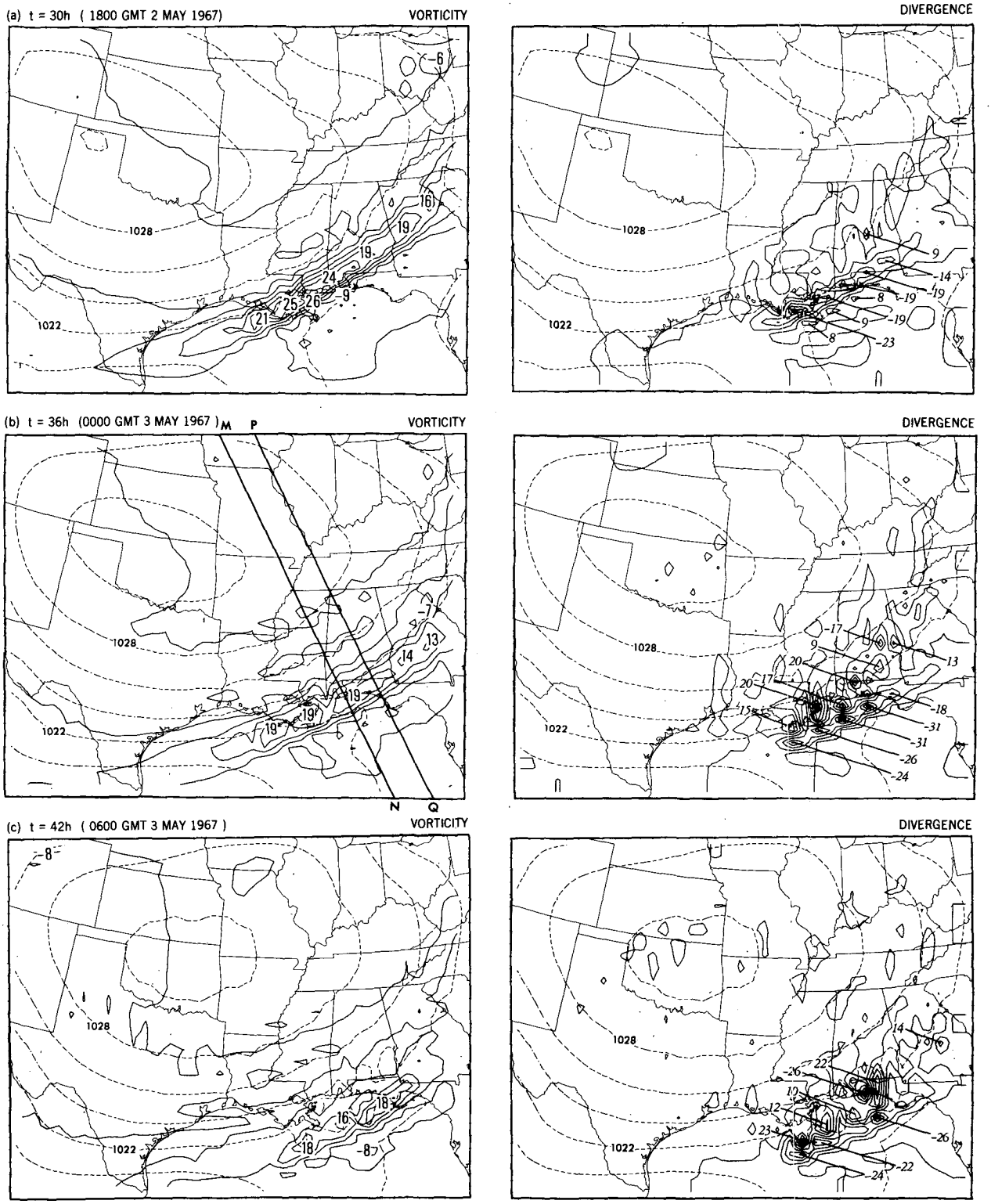

FIG. 6. Maps of vertical vorticity (left frames) and horizontal divergence (right frames) at the surface from the moist solution at three different times. Both vorticity and divergence values are shown in units of 10^{-5} s^{-1}. Contour intervals $\Delta\zeta = \Delta\mathcal{D} = 5 \times 10^{-5}$ s^{-1}. Surface pressure (dashed contours) is shown for reference purposes with a contour interval of 2 mb. Line segment MN as in Fig. 2. Line segment PQ indicates the orientation of the vertical cross-sections in Figs. 11–15, 17–18 and 25–29.

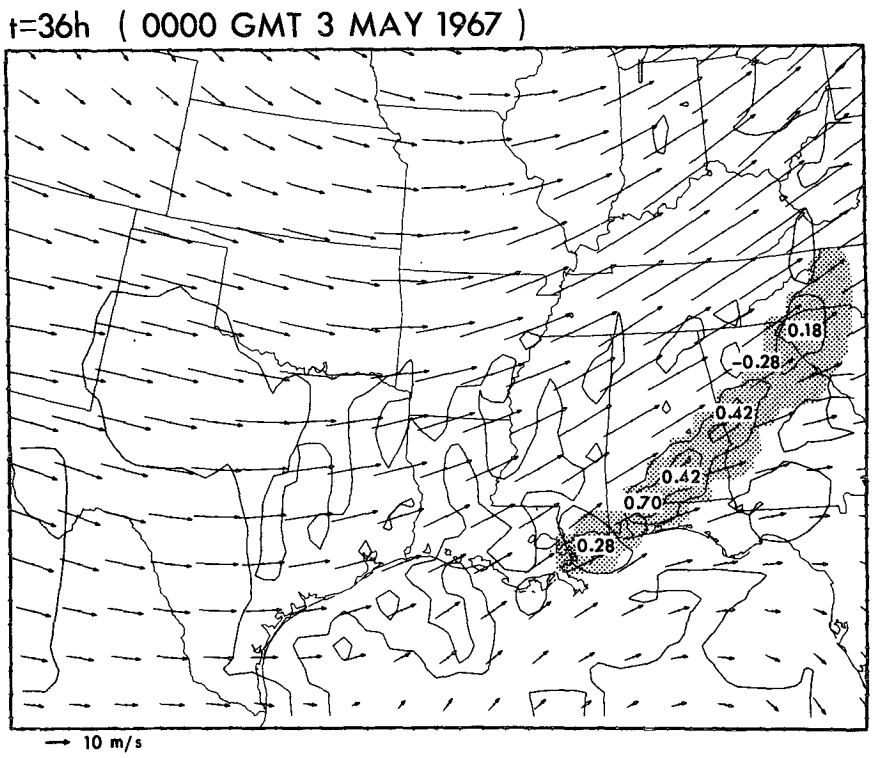

FIG. 7. Composite map from the moist solution at a height of 5000 m showing horizontal wind vectors (see scale in lower left corner), region of cloudwater (stippling), and vertical velocity w (contour lines with $\Delta w = 0.2$ m s^{-1} and extrema labeled).

vergence pattern at 42 h in Fig. 6. A careful comparison of the vorticity curves at 42 and 48 h between Figs. 3 and 9 reveals that the dry front vorticity pattern (centered at 1200 km) has reappeared in the moist-case distribution to the rear of the convectively-induced peak. It is conjectured that the line of convection has moved ahead of the surface front along the cross-section MN at this time; however, the model resolution and difficulties in defining the position of the surface front make it hard to confirm this hypothesis conclusively.

3. Structure and dynamics of the moist convection

As we have seen in Section 2b, the deep convection which the model resolves explicitly is the major change

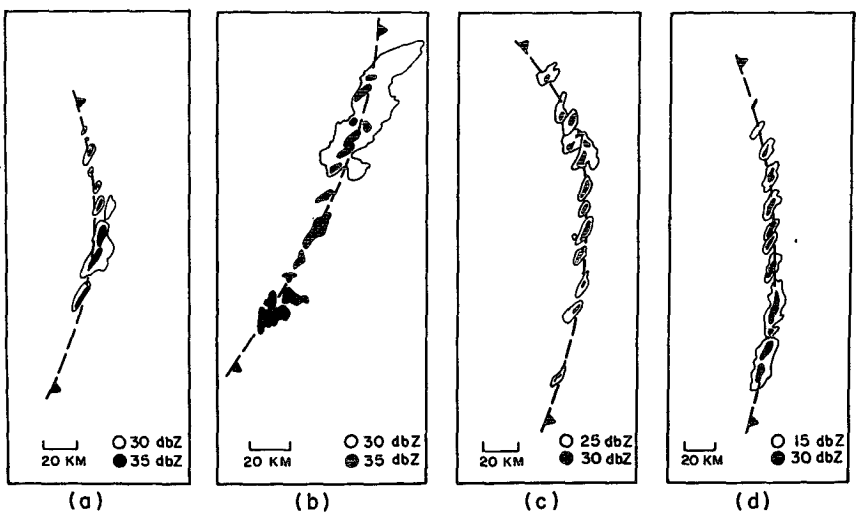

FIG. 8. Reproduction of Fig. 1 of Hobbs and Biswas (1979) showing small mesoscale horizontal structures of narrow cold-frontal rainbands as observed by radar with 1° elevation angle (courtesy of P. Hobbs).

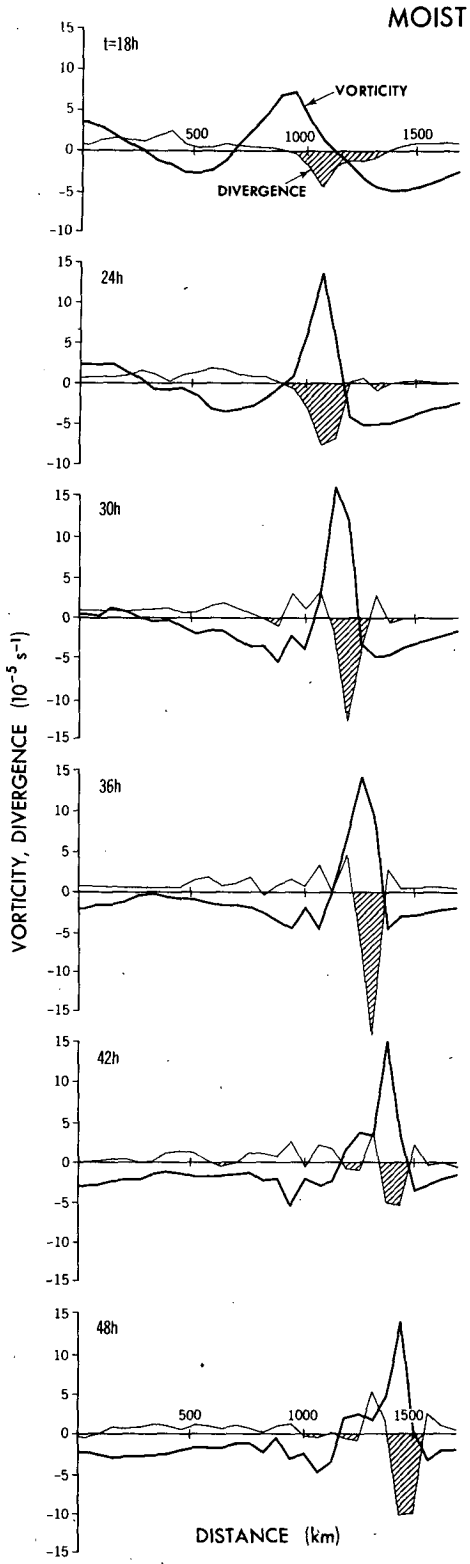

FIG. 9. As in Fig. 3, but from moist solution.

which occurs when moisture is included in the solution. In the present model, the moist convection, both stable and unstable, is represented directly by the model equations; that is, the heat released during condensation produces a decrease in the hydrostatic pressure in the column, thereby enhancing the convergence in the column and producing convective lifting. However, since the grid scale of the model is too large to produce efficient convection, the vertical penetration of the simulated convection is enhanced through the use of a nonlinear vertical eddy diffusivity which is a function of Richardson number and vertical velocity (see Section 2 of RO for details).

There are several reasons why an explicit representation of convection, rather than some form of convective parameterization, has been chosen for use in the present model. First of all, the present approach is more straightforward and unambiguous to use compared to the use of more complex cumulus parameterizations. As Rosenthal (1979) has found from experiments conducted on a hurricane simulation, different aspects of a mesoscale simulation can be quite sensitive to the somewhat arbitrary choice of parameters needed for different cumulus parameterizations. Hence, in the absence of a more rigorous physical justification with which to choose the detailed form of a cumulus parameterization, it seems prudent to employ an explicit convective representation in the present mesoscale model. In addition, explicit convection has the benefit that it allows the transport of momentum and heat within the convective zone, as well as the excitation of gravity waves, to occur directly within the dynamics of the model equations. Also, the time scale for the development of convection is more gradual than the nearly instantaneous change which occurs in adjustment-type parameterizations which are more suited to general circulation models. Finally, a more practical advantage of the present approach is that the representation of convection in the model will become more and more realistic as numerical simulations are nested to smaller and smaller scales, so long as nonhydrostatic and quasi-hydrostatic (Orlanski, 1981) forms of the model equations are used as necessary. (A prognostic equation to predict rainwater phase should also be added to the present system of equations.)

a. Description of convective activity

Although the convection is shown from the divergence in Fig. 6 to be aligned with the front, its structure is highly variable in the vertical along the surface front, as shown by the three-dimensional display in Fig. 10. The vectors showing surface winds in this figure indicate winds to be northeasterly on the cold air side of the front and convergence of tracers along the frontal zone. The southerly winds in the warm sector, which supply moist air from the Gulf of Mexico to maintain the frontal convection, are less evident than in the streamlines of Fig. 5.

In spite of the three-dimensionality of the convective zone, we will find it very instructive to display the

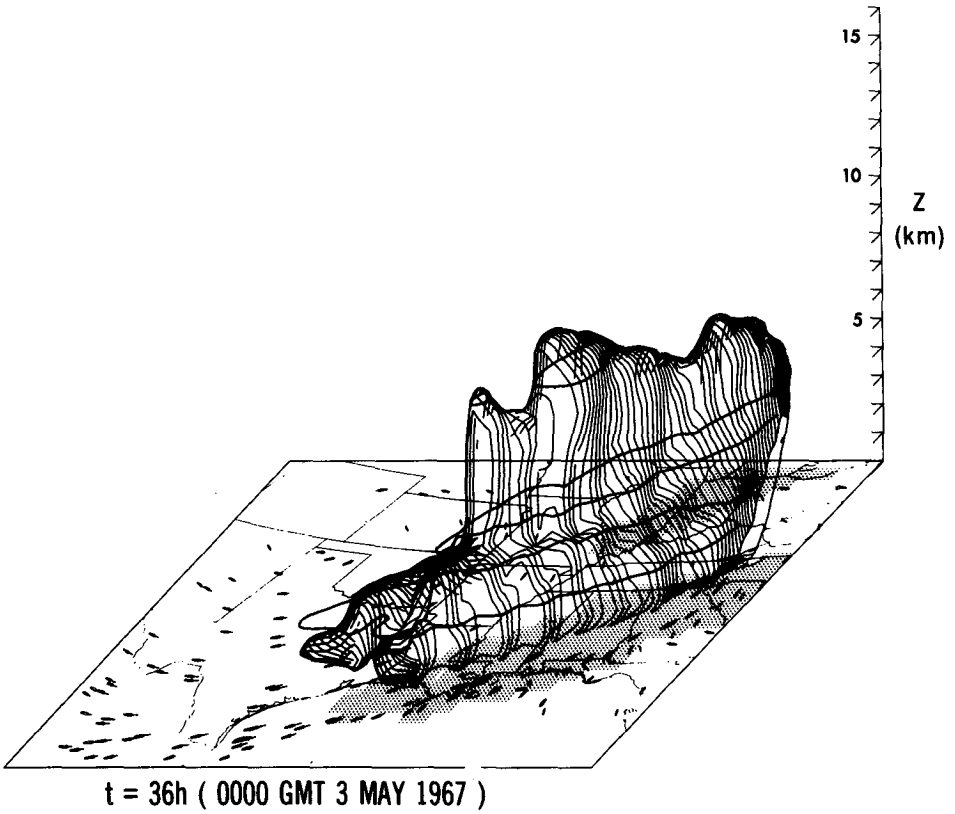

FIG. 10. Three-dimensional structure of cloudwater field from the moist solution at 36 h. Stippling at the surface indicates regions where precipitation has occurred. Vectors at the surface show local wind direction of randomly placed tracers.

evolution of the winds, temperature, and cloud water in the vertical slab aligned with the cross-section PQ shown in Fig. 6. Cross-section PQ, like MN, is approximately perpendicular to the front and the associated maximum vorticity and divergence lines during the time period from 18 to 48 h in the simulation. (Cross-section PQ is used here rather than MN because convection begins earlier and persists for a longer time along PQ.) Figures 11–13 show the time history of the development and decay of convection within this slab during this 30 h period at 6 h intervals.

Figure 11 shows the cross-section for the first two times, 18 and 24 h. The cloud first appears around 18 h as a result of forced convection ahead of the nose of the cold front.[1] As the convection develops, the surface convergence at 24 h is enhanced beneath the convective zone, which now penetrates to a depth of 4 km. The vertical component of cyclonic vorticity, which is apparent in Fig. 11 as the rightmost gradient of the northeasterly surface jet, is also intensified beneath the cloud due to vortex stretching produced by the convection-induced convergence.

As discussed in the previous section, the moist air feeding the cloud at this stage originates in the warm air ahead of the front over the Gulf of Mexico. This air, which is drawn up into the shallow convective zone, exits above the cloud at ~5 km in both directions. Sinking motion occurs to the rear of the front, enhancing the basic vertical ageostrophic circulation associated with the dry frontal system.

At 30 h (Fig. 12), the convection is penetrating into the upper troposphere, with convergence and horizontal shear in the jet beneath the cloud increasing further. At this point, several important features are evident in the structure of the convection. First, the maximum updraft inside the cloud occurs on the warm air side of the convective zone at lower levels and in the center of the cloud at middle levels. Also, above the cloud intense vertical downward motion is excited as an apparent gravity-wave response to the unsteady convective development. Finally, the dry air entering

[1] Replacement of the free-slip surface boundary condition with a bulk drag condition as described in Section 2a was shown to weaken the frontal convergence and thereby to delay the appearance of a cloud. This weakening of the frontal lifting was also found by Keyser and Anthes (1982) when they used a bulk drag surface boundary condition in a dry two-dimensional frontal simulation. However, their finding that a more realistic planetary boundary layer (PBL) representation enhances the low-level frontal lifting suggests that adequate resolution of the PBL in the present case may hasten cloud formation.

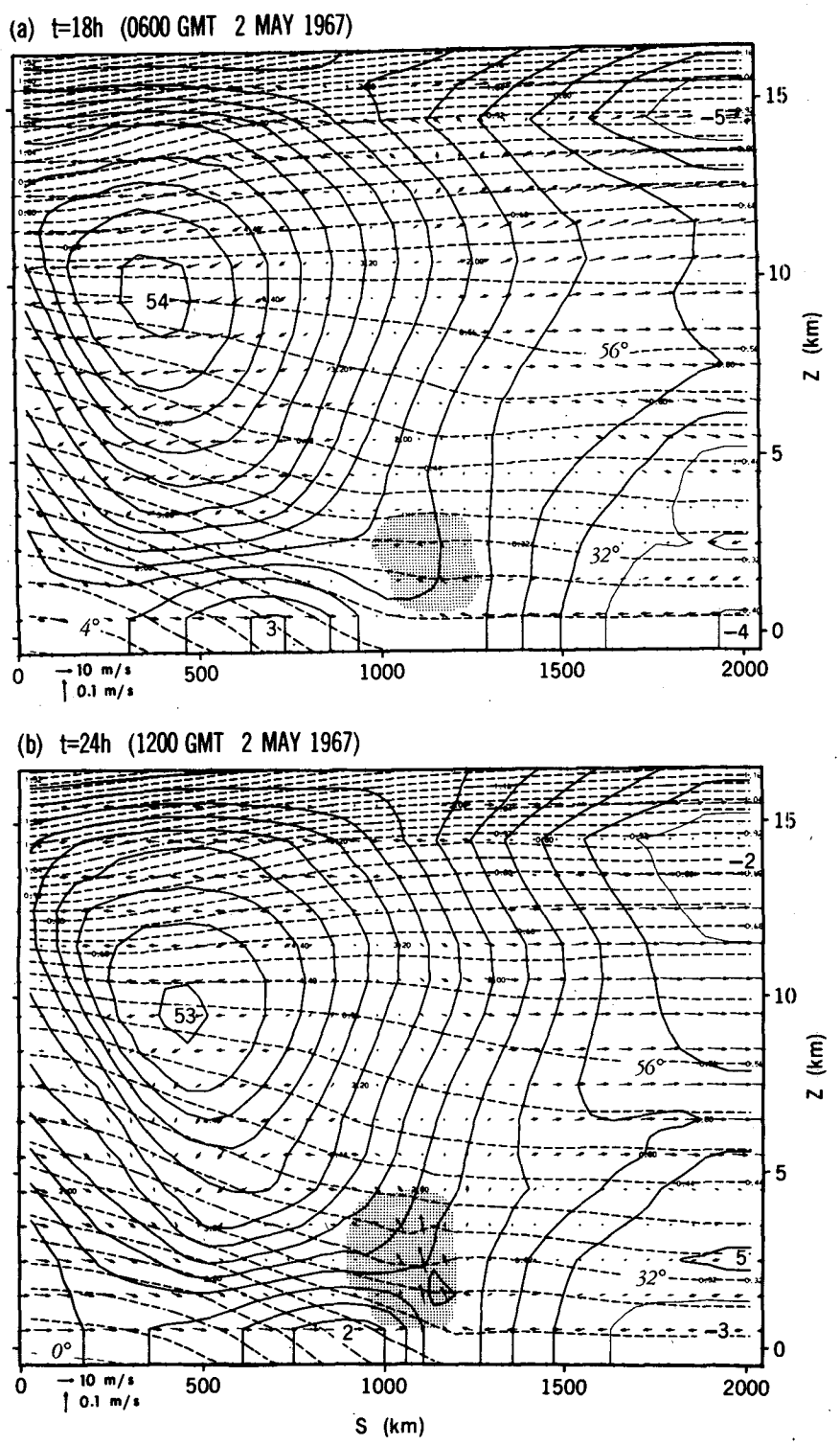

FIG. 11. Vertical cross-section oriented along the line segment PQ shown in Fig. 6b, for 18 and 24 h. Horizontal distance S is measured along this line with the origin at the northern point P. Vectors indicate motion in the plane of the cross-section (refer to scales in lower left corner), while solid contours indicate velocity perpendicular to the cross-section (contour interval of 4 m s^{-1} with extrema labeled). Dashed lines show potential temperature (contour interval of 4 K with some contours labeled in italics). Stippling indicates regions of cloudwater.

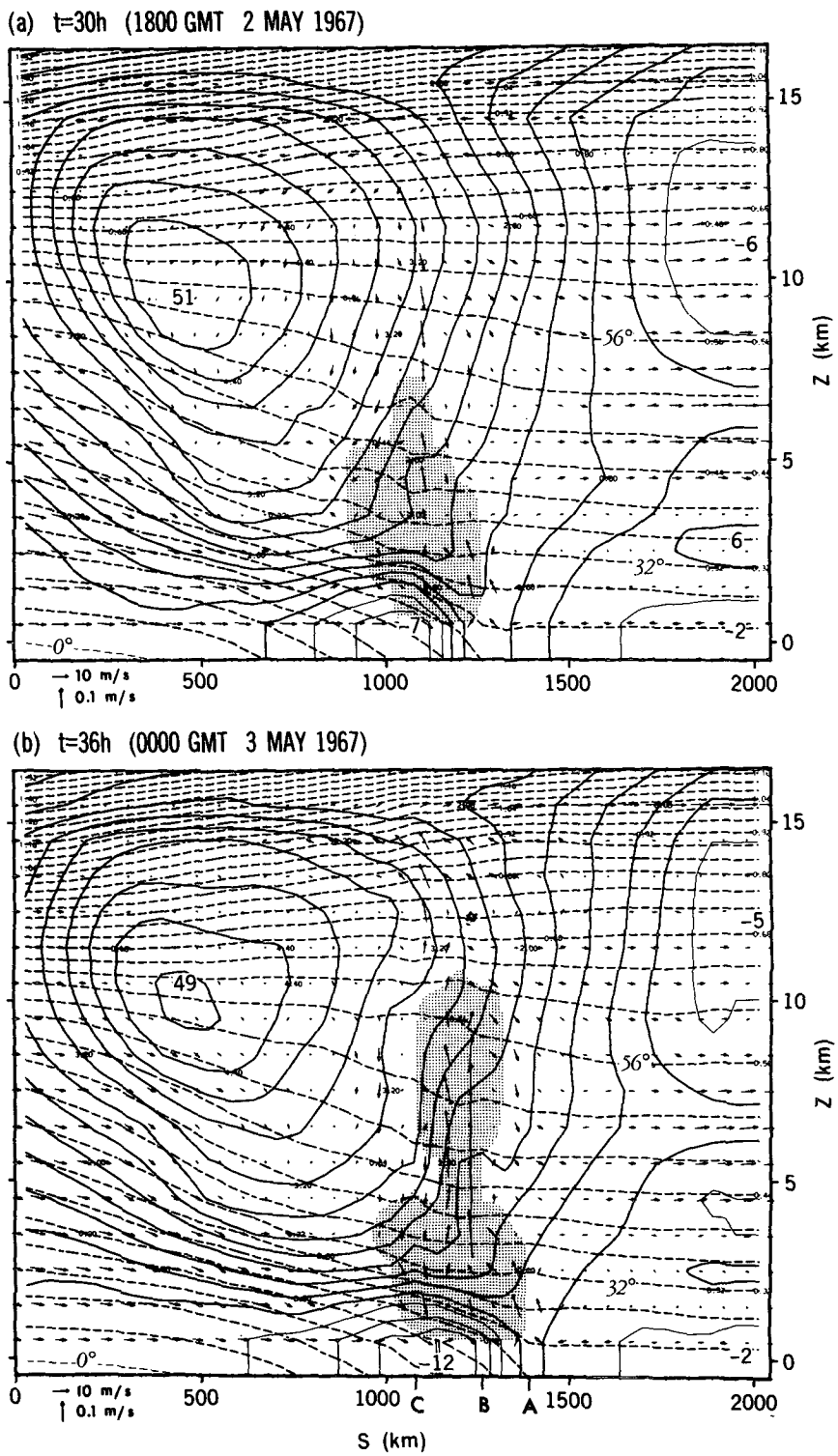

FIG. 12. As in Fig. 11, but for 30 and 36 h. Letters A, B and C along the lower boundary of (b) show the positions of the soundings shown in Fig. 16.

the convective zone behind the cloud at ~2–3 km is associated with a secondary convergence region along the cold air side of the system. We will show later in this section (Figs. 14 and 15) that part of this air is drawn into the updraft of the cloud while the remainder is swept into the downdraft beneath the cloud.

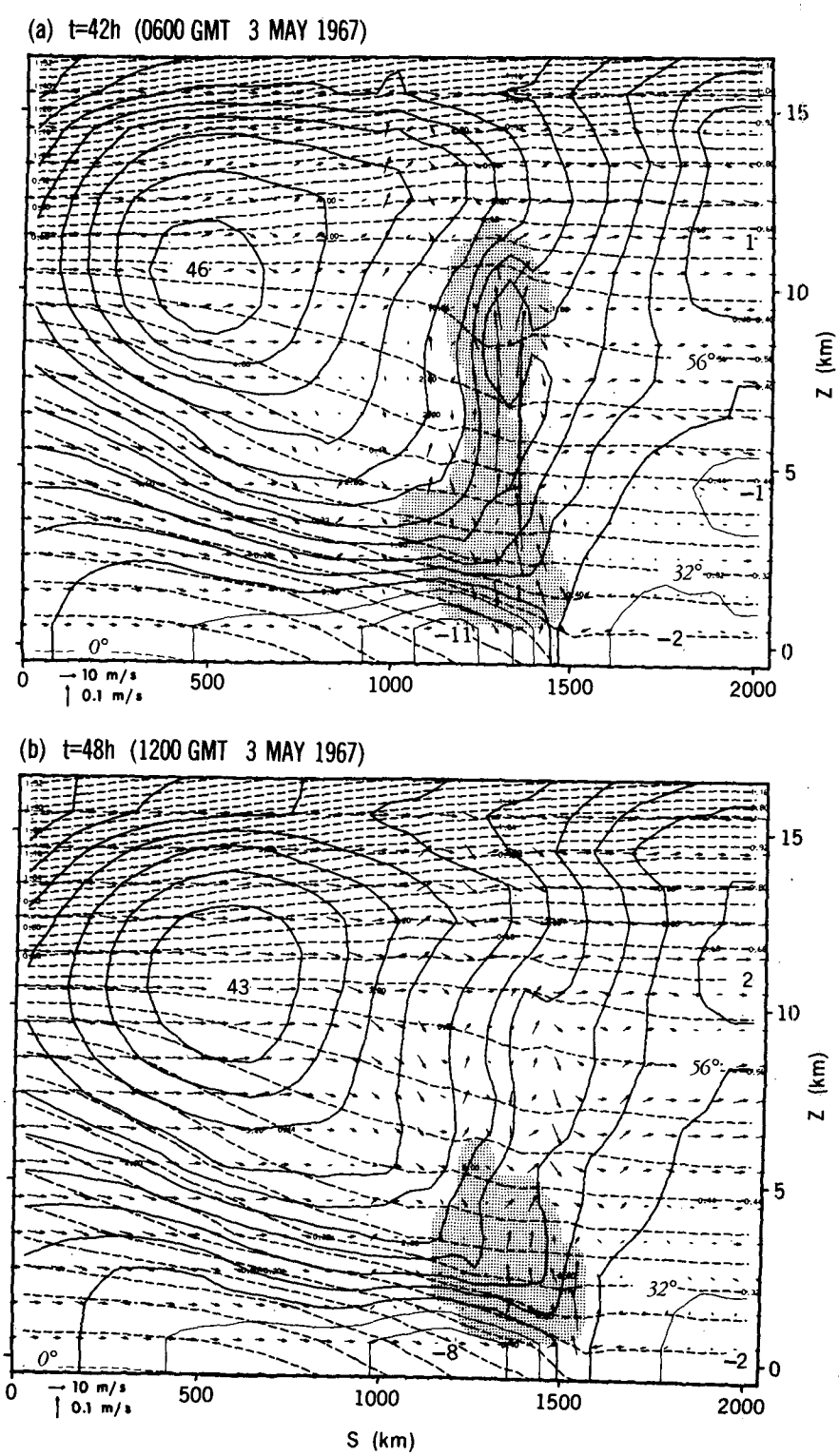

FIG. 13. As in Fig. 11, but for 42 and 48 h.

The vertical circulation typical of a mature squall line is evident in the 36 h cross-section of Fig. 12. The low-level updraft occurs in the forward edge of the squall line. In the middle levels at around 5 km, the updraft is located in the center of the cloud. Finally, air exits the cloud zone at 11 km, producing downdrafts

in the clear air on both sides of the cloud. A convergence zone persists at around 3 km toward the rear and center of the low-level cloud zone. Air enters the rear of the cloud zone both as a downgliding flow along the frontal isentropes and as a downdraft from the convective system above. Part of this air at the rear of the cloud is then directed downward and forward toward the nose of the front to further enhance the initial surface convergence.

In the 36 h cross-section, the deep penetrative convection interacts strongly with the upper-level environmental wind normal to the plane of the cross-section. The horizontal anticyclonic shear in the jet stream to the rear of the cloud is shown to be enhanced as the convection produces vortex stretching within this shear zone. The wind field is distorted further at 42 h (Fig. 13) as the convection penetrates to a depth of 12 km.

At 48 h, the convection within the cross-section has collapsed. As a result, the stable air above the cloud shows oscillations in velocity and temperature which suggest the presence of gravity waves. At the same time, the distortion of the environmental winds is reduced.

Maximum vertical motion near the surface appears to be located somewhat ahead of the line of maximum surface vorticity (indicated by large $\partial v/\partial x$), as was also indicated by Fig. 9. This suggests that the squall line has moved ahead of the surface front, although this cannot be conclusively demonstrated because of the coarseness of the horizontal resolution.

The vertical circulation within the front and convective zone can be better visualized by displaying streamlines within the vertical cross-section. A comparison of these streamlines between the dry and moist simulations is shown in Figs. 14 and 15 for the solution times 30 and 36 h, respectively (compare with Fig. 12 for wind, temperature and cloud patterns). As both figures indicate, the streamline patterns of both dry and moist solutions are remarkably similar away from the convective region. At 30 h, downward motion beneath the jet stream and the flow down the isentropes along the frontal surface are clearly similar in both dry and moist cases. Even the surface convergence occurs at the same position. On the other hand, the convergence intensity and the pattern of circulation in the cloud area is modified in the moist case. It was observed earlier that two updrafts form within the convection zone, one a low-level updraft on the leading edge of the zone and the other a midlevel updraft in the center of the convection region. This feature is clearly evident in Fig. 14.

The convective circulation is deeper and more intense at 36 h (Fig. 15) when the convection is fully developed. In addition, part of the air which exits the updraft at 9 km forms a downdraft on the rear side of the cloud zone. This downdraft air then mixes with the dry air which enters the cloud zone from the rear. (Note that this downdraft is not associated with rainwater loading because a rain phase is not included in the present model.) The resulting low-level flow then enhances the low-level updraft. A separate midlevel updraft is still evident in Fig. 12 at 36 h.

b. Comparison of convective structure with that of an observed squall line

It is not possible to verify the structure of the simulated squall line with that which was observed on 2–3 May 1967 because of the absence of mesoscale upper-air data during that period. However, it is useful to compare our results with the structure of an observed midlatitude squall line as analyzed by Ogura and Liou (1980). The observed squall line passed over the mesonetwork of the National Severe Storms Laboratory in central Oklahoma on 22 May 1976. Unlike the squall line in the present study, the observed Oklahoma convection did not have a synoptic-scale cold front associated with it. However, as we will show in the comparisons which follow, the structure of this observed convective system exhibits a surprising number of similarities to the simulated frontal squall line being studied here.

Before making a direct comparison of the vertical structure of the simulated and observed squall lines, we will first look at temperature–dew-point profiles at different positions in the vicinity of the convective region in the moist simulation. Figures 16a, b and c show adiabatic chart profiles taken from the moist solution at 36 h at positions along the cross-section PQ ahead of the convection, and at forward and rear positions within the convective zones. The respective horizontal positions of these "soundings" are indicated in Fig. 12 at 36 h by the letters A, B and C. In sounding A immediately ahead of the cloud zone (Fig. 16a), the environment is shown to be conditionally unstable from the surface to 1.5 km and from 5 to 8 km with a lifted index of −2. Above the surface vorticity maximum at position B (Fig. 16b), the profile of relative humidity on the left side of the plot indicates that the column is saturated (95% relative humidity for the model) from 1.5 to 3.5 km and from 6.5 to 10 km. The height of the cold front surface is apparent at 1.5 km as a point of discontinuous lapse rate. The sounding at the rear of the convective region (Station C, shown in Fig. 16c) shows saturation occurring from 1.5 to 4.5 km with the cold frontal surface appearing at a height of 2.5 km. Note that the air below and above the cloud zone is quite dry at this position. Some similarity exists between the shape of the low-level temperature and dew point curves in sounding C of Fig. 16, and the "onion shaped" sounding in Fig. 27 of Ogura and Liou (1980) for a position to the rear of their observed squall line. However, the cold air occurring close to the ground in their case probably results from the evaporation of rainwater, a cooling mecha-

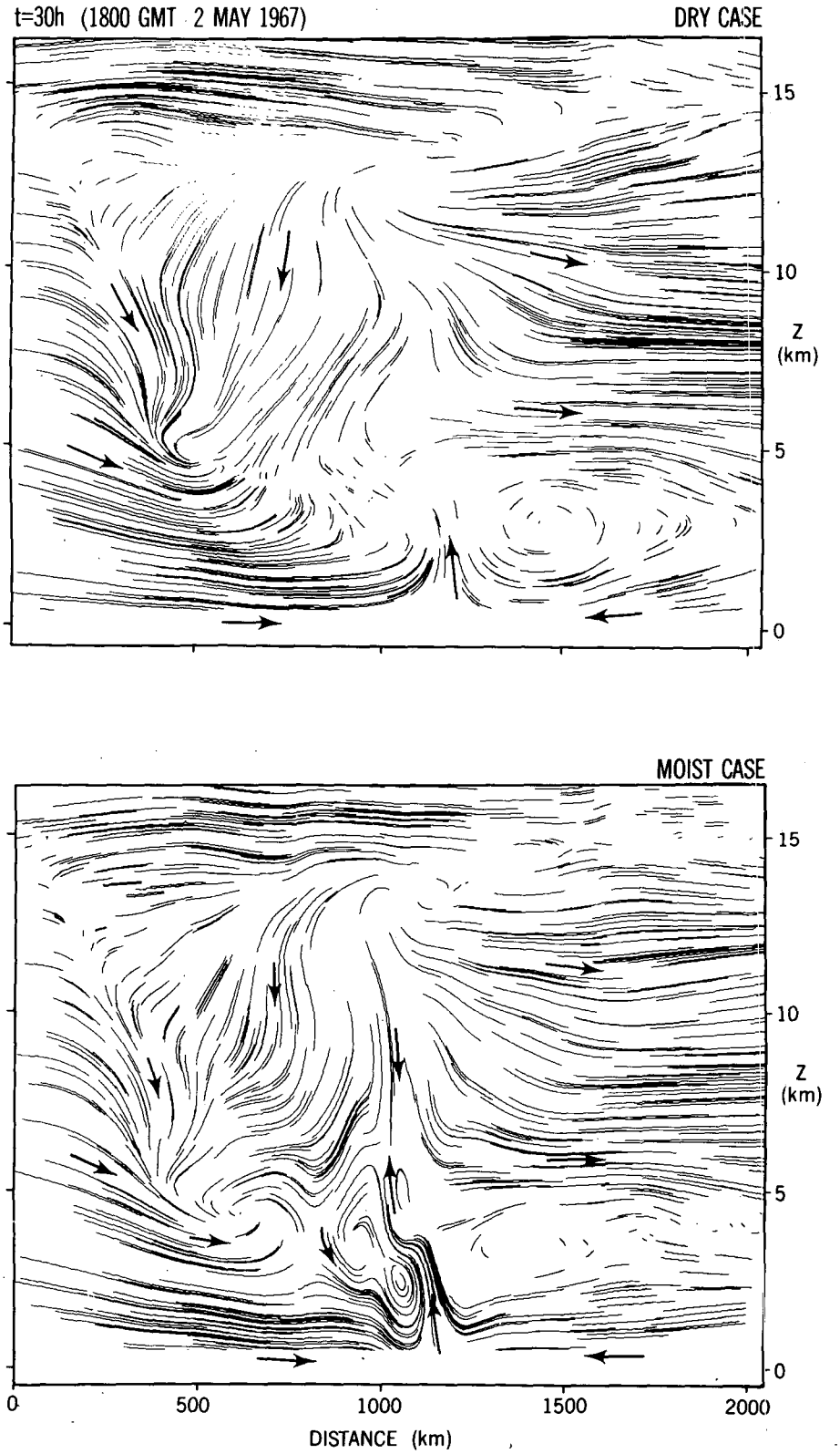

FIG. 14. Streamlines in the same vertical cross-section as Figs. 11–13 for the dry (top) and moist (bottom) cases at 30 h.

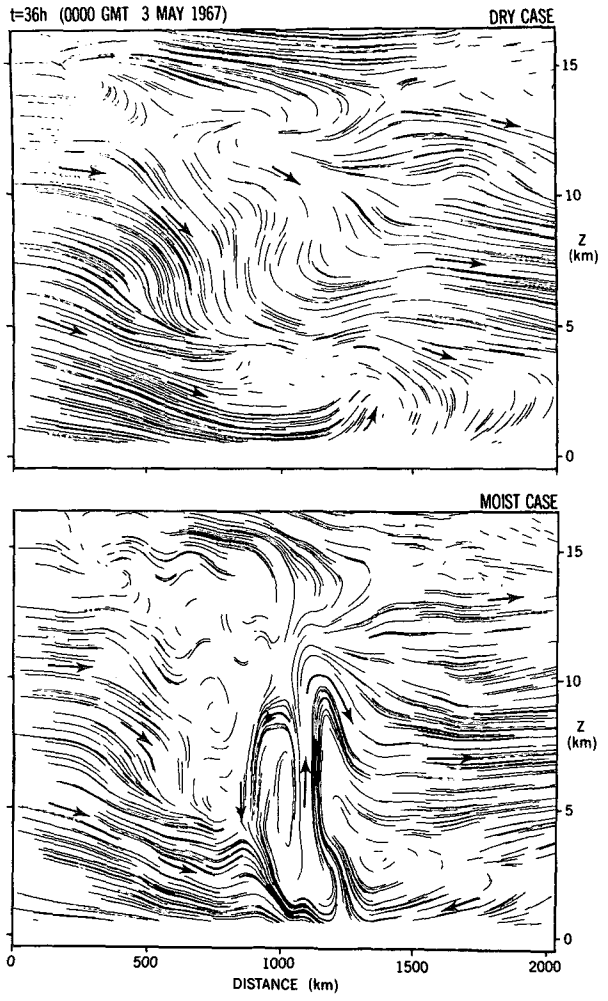

FIG. 15. As in Fig. 14, but for 36 h.

nism which is not possible in the present form of our mesoscale model.

A comparison can be made between the vertical structure of the present modeled squall line and the Oklahoma squall line. Figure 17 shows a comparison of cross-sections of horizontal divergence, vertical velocity and vertical vorticity between the observed squall line (reproduced from Figs. 15, 16 and 18, respectively, of Ogura and Liou, 1980) and the simulated squall line along the segment PQ (see Fig. 6). Corresponding frames are adjusted so that maxima in surface vorticity (i.e., surface wind shift lines) are aligned with each other (both with an abscissa value of 0 km). Note in Fig. 17 that the observed (upper row) and simulated (lower row) fields differ in that the observed fields use pressure P and pressure tendency ω for vertical coordinate and vertical motion, respectively, while the model fields use physical height z and vertical velocity w.

The fields of divergence exhibit a number of similarities between the observed and simulated cases. Maximum values of convergence occur at midlevels approximately 120 km to the rear of the surface maxima in both cases. The magnitudes of the midlevel and surface convergence maxima in the simulation are roughly half the corresponding observed values. However, the occurrence of these two extrema in the observed case seem to support the dual updraft structure which Fig. 13 revealed in the moist solution. A divergence maximum exists below the midlevel convergence maximum in both cases although its intensity in the simulated case is less than half the observed value. The tops of both squall lines, as indicated by the heights of the divergence zone above the midlevel convergence region, appear to be around 200–250 mb, which is approximately the tropopause level.

As might be expected, the vertical motion in the simulation shows the similarities to the observed ω field that were indicated by the divergence comparison. A midlevel updraft occurs above a low-level downdraft, both of which are displaced 120 km behind the leading low-level updraft. The observed downdraft, which is probably induced by water loading and evaporative cooling in the Oklahoma squall line, is considerably more intense than its counterpart in the simulation, which does not have the benefit of rainwater evaporation.

Similarities between vertical vorticity cross-sections in Fig. 17 are not as extensive as they are for divergence and vertical motion. The occurrence of a zone of cyclonic vorticity at the surface in the simulation does not agree with the observed case although the former has half the intensity of the latter and is considerably broader in extent (reflecting the horizontal scale of the surface cold front). In both cases, the axis of maximum cyclonic vorticity tilts upward to the left from the surface maximum. Also, a region of anticyclonic vorticity occurs above the cyclonic surface vorticity in both cases.

The major difference between the two cases in Fig. 17 occurs in the midlevel vorticity pattern to the rear of the surface maximum. Although divergence patterns were shown to be quite similar in this region, the vorticity fields indicate opposite signs. The simulation shows an anticyclonic field at this location, which results from an enhancement of the horizontal shear in the southwesterly jet stream due to the penetrative convection of the squall line. No mechanism is available to explain the cyclonic vorticity which occurs in this region in the observed case, although it is possible that vortex stretching due to midlevel convergence might have caused this, as suggested by Ogura and Liou (1980).

c. Nondispersive constraints on the environment of a convective system

Over the period in which a convective cell develops and then decays, the surrounding environment should

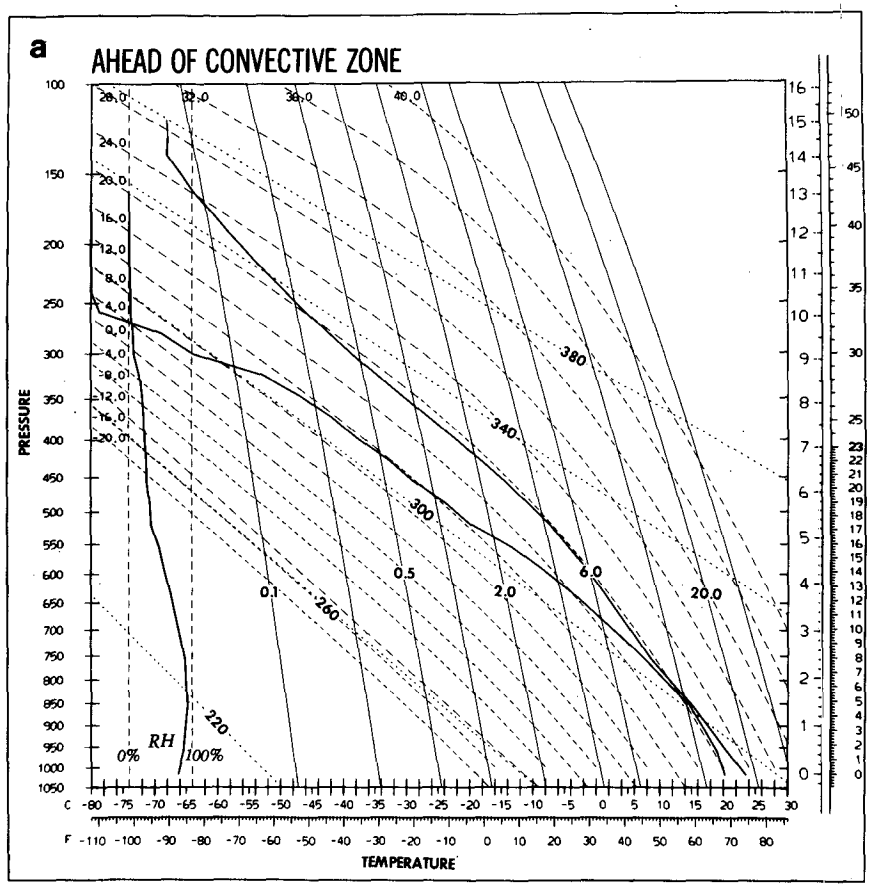

FIG. 16a. Model "sounding" taken in the moist solution at 36 h along the line PQ (Fig. 6b) at position A only shown in Fig. 12. The plot shows a standard pseudoadiabatic chart with ordinates of pressure (mb) on the left and height (km and 10^3 feet) on the right. Temperature (°C and °F) is the abscissa. Plotted lines to the right are temperature (upper curve) and dew point temperature (lower curve). Relative humidity is shown to the left between the dashed vertical lines which designate 0 and 100%. Background lines indicate constant saturation mixing ratio (nearly vertical, light solid lines), pseudoadiabats (sloping dashed lines) and dry adiabats (sloping dotted lines).

exhibit a gravity-wave-like response similar to that found experimentally by Cerasoli (1979). In fact, the numerical simulation presented here shows small-scale convective elements growing and decaying within the convective region and thereby producing gravity waves in the air above. We will show in the discussion which follows that certain horizontal gravity-wave scales will be favored in long-lived convective systems.

It is well known that solitary waves can exist for many times their intrinsic period because of their nondispersive characteristics. If a convective system is to survive for a similar period of time in a stably stratified environment, it must likewise be in dynamic balance with the surrounding stable fluid. Otherwise, the penetrative convection within the system will produce a field of dispersive gravity waves which will carry away much of the energy from the organized system and destructively interfere with the organization of the system. If a convective region is to maintain its organized structure, it not only must maintain the low-level moisture source which sustains its convection, but it also must have a physical structure and propagation speed which is consistent with a solitary wave which exists in the surrounding stable environment. Two requirements are necessary if this compatibility is to occur: First, the speed of the convective system should be similar to the group velocity of a solitary wave, and second, the aspect ratio H/L of the horizontal to vertical scales of the system should be compatible with such a nondispersive wave. The second condition, requiring the nondispersive character of the waves, defines the horizontal scale for such storm systems. Specifically, gravity waves will be dispersive when their horizontal wavelengths are either too short or too long. If the wavelength is too long, Coriolis effects will be important, and the waves will propagate away as dispersive

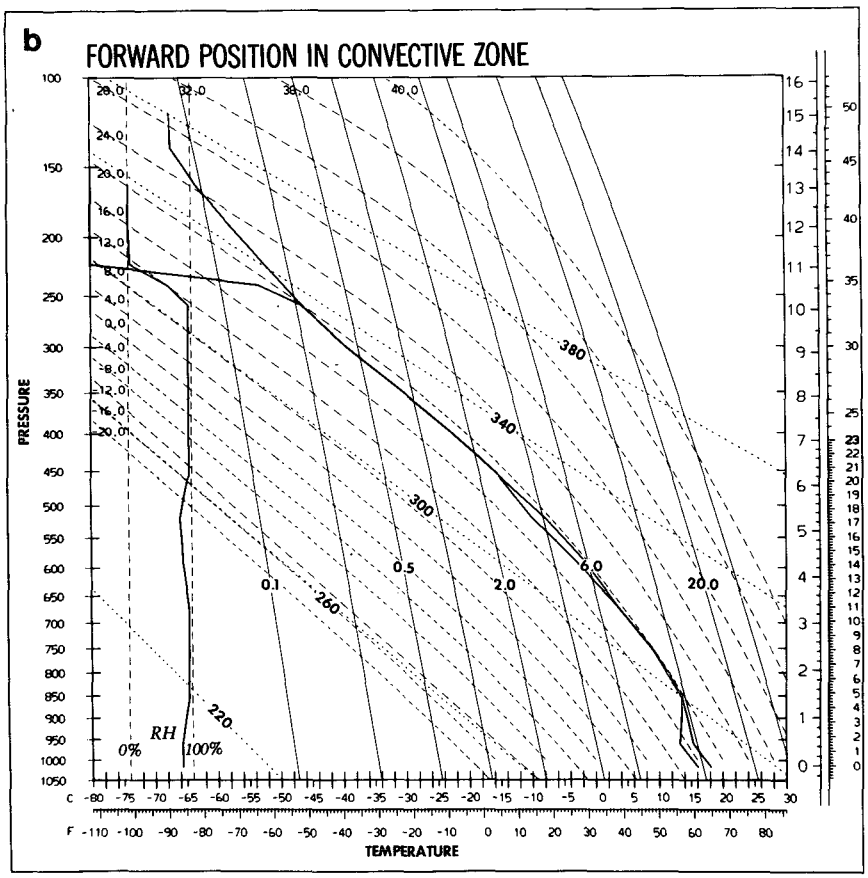

FIG. 16b. As in Fig. 16a, but for position B shown in Fig. 12.

inertial-gravity waves. On the other hand, if the wavelength is too short, nonhydrostatic effects will again make the waves dispersive. Hence, reference to the dispersion relation for internal gravity waves in a rotating system allows us to specify limits on the aspect ratio H/L so that gravity waves will be nondispersive, namely

$$\frac{f}{N} \ll \frac{H}{L} \ll 1, \tag{3.1}$$

where N is a representative Brunt–Väisälä frequency. With typical values of f and N for the atmosphere of 10^{-4} and 10^{-2} s^{-1}, respectively, and an assumed height H of 10 km for a convective system, the horizontal scale L of the nondispersive system will be given by 10 km $\ll L \ll$ 1000 km. The horizontal scales of most organized mesoscale systems lie within this range.

In fact, the horizontal scales L of most organized mesoscale systems lie within the range $H \ll L \ll \lambda_R$, where λ_R is the Rossby radius of deformation NH/f. This scale range is quite broad; however, attempts to refine the scale have been unsuccessful. In particular, Emanuel (1982) has suggested, in a study of symmetric instability, that the characteristic length of the most unstable symmetric wave is $\lambda_s = u_z H/f$. However, the argument which he uses assumes that the Richardson number $\mathrm{Ri} = N^2/u_z^2 \approx 1$; therefore his length scale λ_s is essentially the same as the Rossby radius of deformation λ_R.

A more fruitful approach to this scaling problem assumes that the characteristic horizontal scale for large mesoscale disturbances is, in fact, λ_R, but with a smaller Brunt–Väisälä frequency N. This value of N would be one which is more representative of the less stable mesoscale environment rather than a value appropriate for planetary scale waves. From a supportive point of view, one may argue that while the vertical shear u_z is similar for both the planetary and mesoscale environments, the bulk Richardson number varies from values on the order of 100 for larger scales to unity for mesoscale convective systems. In fact, the depth of the atmosphere over which the Richardson number is of order unity will typically be much less than the tropopause height H, which would be appropriate for the radius of deformation λ_R of large-scale processes. Therefore, the assumption that Ri be of order unity can only be justified in a shallower layer of the at-

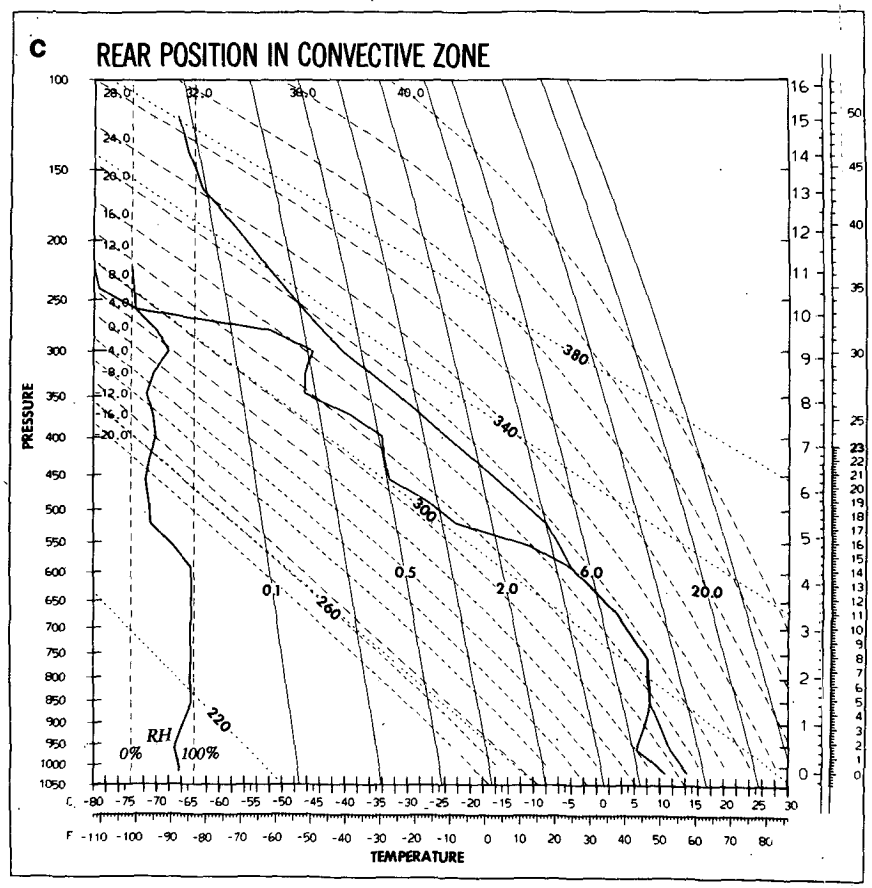

FIG. 16c. As in Fig. 16a, but for position C shown in Fig. 12.

mosphere. Use of this decreased depth to calculate λ_R would thus further reduce the characteristic horizontal scale of mesoscale phenomena in comparison to the radius of deformation for larger scale disturbances.

d. Balance of vertical advection and diabatic heating

In the Appendix the distribution of terms from the equations of motion is presented for the moist numerical solution at 36 h in a vertical cross-section oriented perpendicular to the surface front (line PQ of Fig. 6). The reader is referred to the Appendix for an explanation of how these terms were obtained from the numerical solution. Although we will not consider the details of these terms beyond the discussion of the present subsection, we present them in the Appendix in the hope that they will be of use to researchers studying the dynamics of a well-documented observed front.

Because the model treats convection in an explicit manner, the form of the temperature and water vapor tendency equations within the cloud zone are of special interest. As Figs. 27 and 28 in the Appendix will show, the time rates of change of both θ and q are quite small within the cloud region, indicating that the convective system along this cross-section is in a quasi-steady state. (The large negative tendencies which appear above the cloud zone are apparently the result of gravity waves produced by the penetrative convection.) While the temperature is approximately steady within the cloud region, strong diabatic heating is occurring in the two cloud updrafts.

Figure 18 shows a more detailed comparison (taken from Figs. 27 and 28) of the terms for vertical advection of θ and q and the diabatic heating and evaporation terms within the cloud zone at 36 h. The position of the 0.25 g kg^{-1} contour of cloud water mixing ratio is included in the figure as a dotted line in order to show the location of the cloud zone. This figure indicates that the diabatic heating is closely balanced by the adiabatic cooling due to vertical temperature advection. As a result, the only net heating within the convective region occurs as adiabatic warming to the rear of the midlevel updraft in response to this upward motion. This heating is weakened somewhat by evaporative cooling at the edges of the shallow cloud located to the rear of the convective system. Finally, note in Fig. 18 that adiabatic warming is occurring in the di-

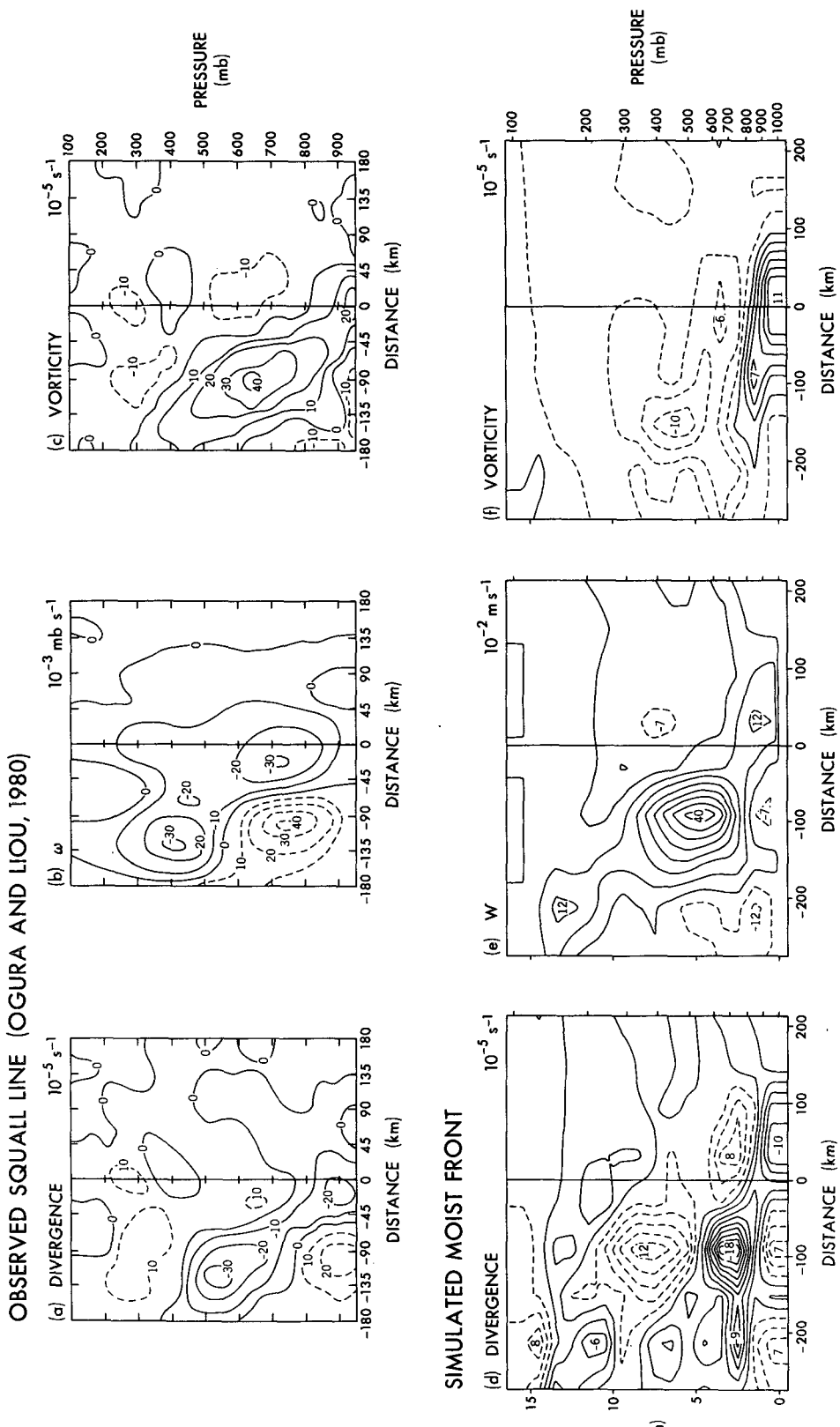

FIG. 17. Comparison of horizontal divergence, vertical motion and vertical component of vorticity between an observed squall line [(a), (b) and (c) are reproduced from Figs. 15, 16 and 18, respectively, of Ogura and Liou, 1980] and the moist front solution within the vertical plane of Fig. 12 at 36 h. The vertical ordinate of (a)–(c) is linear in pressure while that for (d)–(f) is linear in height z. Vertical motion is given by p-vertical velocity ω in (b) and z-vertical velocity w in (e) with solid (dashed) contours indicating upward (downward) motion in both frames. The abscissa, i.e., horizontal distance perpendicular to the squall line, is adjusted so that the origin is located at the position of maximum surface vorticity in both cases.

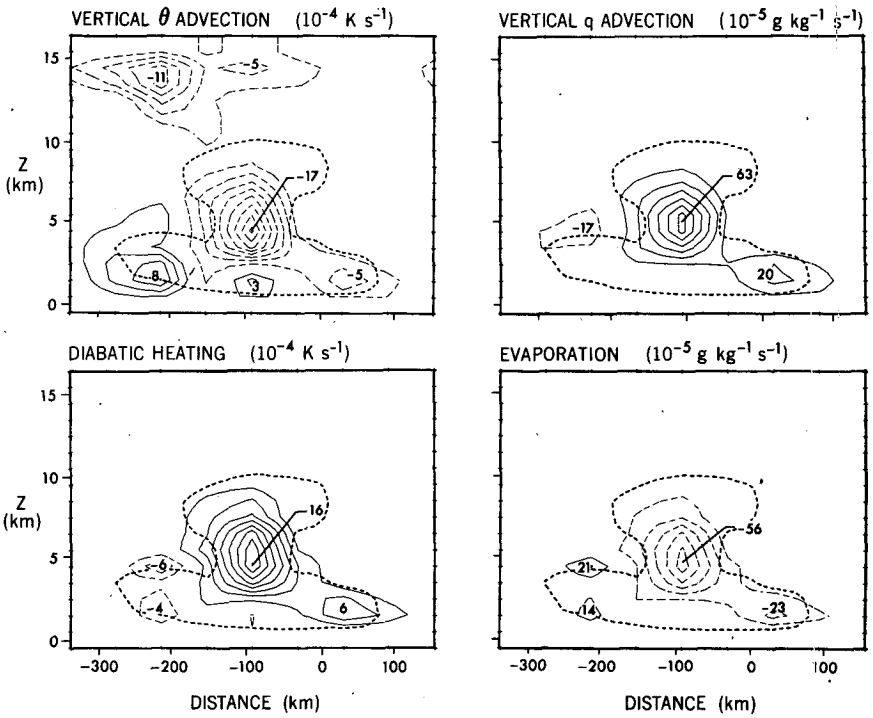

FIG. 18. Comparison of distributions of vertical advection of potential temperature θ with diabatic heating, and vertical advection of vapor mixing ratio q with evaporation, in the vertical cross-section of Fig. 12 at 36 h. Contour intervals are 2×10^{-4} K s^{-1} for θ terms (left frames) and 10^{-4} g kg^{-1} s^{-1} for q terms (right frames). Short dashed contours indicate the position of the 0.25 g kg^{-1} contour of cloudwater mixing ratio. The abscissa is normalized as in Fig. 17.

vergence zone beneath the midlevel updraft. Weak evaporative cooling is occurring at the lower edge of the cloud. This cooling would be more intense if rainwater falling through this region was evaporating, as might be expected from a model which included a rain phase.

The water vapor tendency equation shows a near balance between vertical advection and condensation which is quite analoguous to temperature within the strong midlevel updraft region of the cloud (Fig. 18). This balance is a natural result of the steady-state characteristic of the cloud because any upward advection of q within the condensed water region must cause the advected water vapor to condense in a cloud with a steady saturation mixing ratio field q_s. Also, reference to the rainwater production term in the cloud water tendency equation (Fig. 29) shows this term to have a maximum which is biased toward the top of the region of condensed water production.

4. Linear model of a convective region with low-level wind

One of the major findings of Ogura and Liou (1980) was the existence of strong midlevel convergence zone in the Oklahoma squall line of 22 May 1976, this zone being out of phase with the surface convergence. They attributed the divergence region beneath this midlevel feature to the effects of falling rain, namely evaporative cooling and water loading. Our numerical frontal solution showed a very similar structure of intense midlevel convergence and low-level divergence which is out of phase with the surface convergence; however, the numerical model used in this solution contains no microphysics and thus has no mechanism for evaporative cooling of rainwater beneath the cloud zone and only provides for water loading due to cloud water up to 1.5 g kg^{-1}. This numerical result thus suggests that a simple dry model may be able to explain why the relative location of the surface convergence can be displaced from the midlevel convergence zone in a hydrostatic convective system without the need for microphysics.

In order to better understand the dual updraft structure, we will develop a simple two-layer model to represent the stable and unstable regions in a conditionally unstable atmosphere in which convection is occurring. The model atmosphere is assumed to be dry so as to avoid the complications of moist thermodynamics. Then, in order to simulate the lifting of moist air to a level of free convection, the dry model environment will be divided into two layers, each with constant stratification (Fig. 19). The lower layer is stably stratified ($\theta_{1z} > 0$) and extends from the surface to the level of free convection (LFC) at $z = h$. The upper layer is

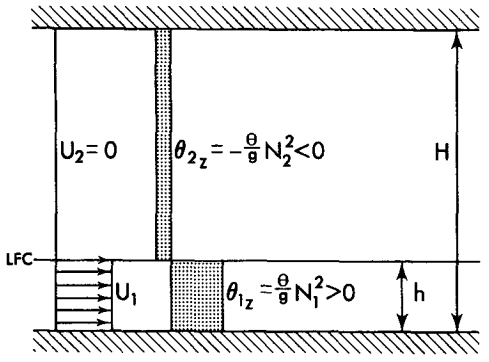

FIG. 19. Schematic diagram showing the configuration of the simple dry model containing two layers, each with constant stratification and uniform winds (the upper-layer wind U_2 is assumed to be zero). The interface between the two layers is viewed as representing the level of free convection (LFC) in the moist environment being modeled.

gravitationally unstable ($\theta_{2z} < 0$) in order to simulate the moist unstable cloud region above the LFC and extends to a rigid lid $z = H$. The lower and upper layers are assumed to have constant mean winds U_1 and U_2, respectively.

A linearized inviscid two-dimensional form of the hydrostatic anelastic equations, described by RO, is assumed to apply:

$$\frac{\partial u'}{\partial t} + U_m \frac{\partial u'}{\partial x} = -c_p \Theta \frac{\partial \pi'}{\partial x}, \tag{4.1}$$

$$\frac{\partial \theta'}{\partial t} + U_m \frac{\partial \theta'}{\partial x} + w' \theta_{m_z} = 0, \tag{4.2}$$

$$0 = -c_p \Theta \frac{\partial \pi'}{\partial z} + \frac{g}{\Theta} \theta', \tag{4.3}$$

$$\frac{\partial u'}{\partial x} + \frac{\partial w'}{\partial z} = 0, \tag{4.4}$$

where subscript m refers to layers 1 and 2, density variations have been neglected and primes denote perturbation quantities.

a. The eigenvalues

A streamfunction ϕ' may be defined to satisfy the continuity equation (4.4). Then, if all perturbation quantities are assumed to vary as $\exp[ik(x - ct)]$ so that $\phi' = \Phi(z) \exp[ik(x - ct)]$, we obtain the following equations by combining (4.1)–(4.3):

$$\frac{\partial^2 \Phi_1}{\partial z^2} + \frac{N_1^2}{(U_1 - c)^2} \Phi_1 = 0 \quad \text{(lower layer)}, \tag{4.5a}$$

$$\frac{\partial^2 \Phi_2}{\partial z^2} - \frac{N_2^2}{c^2} \Phi_2 = 0 \quad \text{(upper layer)}, \tag{4.5b}$$

where, for simplicity and without loss of generality, we have assumed that $U_2 = 0$ and have defined the positive quantities N_1^2 and N_2^2 such that $N_1^2 = g\theta_{1z}/\Theta$ and $N_2^2 = -g\theta_{2z}/\Theta$. Conditions at the rigid boundaries are

$$\Phi = 0 \quad \text{at} \quad z = 0, H. \tag{4.6}$$

Interface conditions at the level of free convection are

$$\Phi_1(h) = \Phi_2(h) \quad \text{(continuity of } w'\text{)}, \tag{4.7a}$$

$$(U_1 - c)\Phi_{1z}(h) = -c\Phi_{2z}(h) \quad \text{(continuity of } \pi'\text{)}. \tag{4.7b}$$

The general solution of (4.5) which satisfies the boundary conditions (4.6) is

$$\Phi_1 = \hat{\Phi}_1 \sin\gamma_1 z \quad \text{(lower layer)}, \tag{4.8a}$$

$$\Phi_2 = \hat{\Phi}_2 \sinh\gamma_2(H - z) \quad \text{(upper layer)}, \tag{4.8b}$$

where γ_1 and γ_2 are complex wavenumbers of the form

$$\gamma_1 = \gamma_{1r} + i\gamma_{1i} = \pm \frac{N_1(U_1 - c_r)}{(U_1 - c_r)^2 + c_i^2} \pm i \frac{c_i N_1}{(U_1 - c_r)^2 + c_i^2}, \tag{4.9a}$$

$$\gamma_2 = \gamma_{2r} + i\gamma_{2i} = \pm \frac{N_2 c_r}{c_r^2 + c_i^2} \mp i \frac{c_i N_2}{c_r^2 + c_i^2}, \tag{4.9b}$$

with $i = (-1)^{1/2}$. Only the upper sign in the above expressions will be used hereafter. Finally, the requirement that (4.8) satisfy the interface conditions (4.7) produces the transcendental equation

$$\tanh\gamma_2(H - h) = -\frac{N_2}{N_1} \tan\gamma_1 h \tag{4.10}$$

which must be solved to determine the complex eigenvalue $c_r + ic_i$ for the eigenfunction (4.8).

Kuo (1963) has discussed the one-layer equivalent of the present model, that is, a fluid of constant stratification having a constant mean wind U, during his investigation of the effect of shear on a stratified fluid. He found that the solution for this case must be of the form of Eq. (4.8a) in order to satisfy the boundary condition (4.6) with the vertical wavenumber γ_1 limited to eigenvalues $n\pi/H$ where n is a positive integer and π/H is the most unstable wavenumber. When the stratification is stable, the perturbation solution is made up of neutral internal gravity waves ($c_i = 0$) whose horizontal phase speeds are Doppler-shifted by the mean current $\bar{U}$.

The behavior of the one-layer model when the stratification is unstable is of special interest here because this will represent the limiting case for the two-layer model in which either the thickness of the lower layer vanishes or the stratification of the lower layer becomes unstable and matches the magnitude of the upper. In this case, the eigenvalue c has a nonzero imaginary part, while the horizontal phase speed of the wave now equals the mean wind $\bar{U}$. Thus, as Kuo points out, all wavenumbers are unstable with the maximum growth

rate kc_i occurring for infinite horizontal wavenumber (because $\omega_i = kNH/\pi$ under the hydrostatic approximation).

A solution for the general two-layer model has been obtained here by using a two-dimensional Newton–Raphson technique (see Hamming, 1962, p. 357) to determine the complex eigenvalues c from (4.10). In the presentation of these results, it is convenient to use nondimensional variables. The natural quantity with which to scale c_i and c_r is $N_2(H-h)\pi^{-1}$, which is the most unstable value which c_i can assume for a single layer of depth $H-h$. We therefore nondimensionalize the eigenvalues as $C_r = c_r\pi N_2^{-1}(H-h)^{-1}$ and $C_i = c_i\pi N_2^{-1}(H-h)^{-1}$. Figure 20 shows the imaginary and real parts of this quantity as a function of the lower level wind U_1 and the stability ratio N_1/N_2, which is denoted by P. The height ratio $\epsilon = h(H-h)^{-1}$ is fixed at a value of 0.1. The maxima in the imaginary part C_i, which occur in this plot for different wind speeds depending upon P, may be interpreted as indicating that a disturbance of a given wavenumber will be most unstable for these particular wind speeds U_1. (As in the case of the single-layer model, the wavenumber with the largest growth rate is infinite in the inviscid model.)

The decrease of the maximum c_i for increasing values of P can be easily understood by the fact that, for small values of N_1 (i.e., small P), the growth rate will be close to that of the completely unstable layer (c_i $= N_2H\pi^{-1}$ when $U_1 = 0$ as studied by Kuo, 1963), which depends upon U_1 as given by the dashed curves in Fig. 20. As N_1 and thus P increases to infinity, the interface at $z = h$ becomes a rigid wall; in this limit, c_i goes to $N_2(H-h)\pi^{-1}$, and the normalized value $c_i\pi N_2^{-1}(H-h)^{-1}$ goes to unity, which is the lower limit of the ordinate in Fig. 20a. Although the curves in Fig. 20 are nearly flat in absolute terms as a function of wind speed U_1, the small relative maxima and minima are apparent in the figure due to the choice of range of the ordinate. The rightmost peak is the most prominent feature; the value of U_1 at which this maximum occurs depends strongly upon the static stability N_1 of the lower layer (assuming N_2 is constant here).

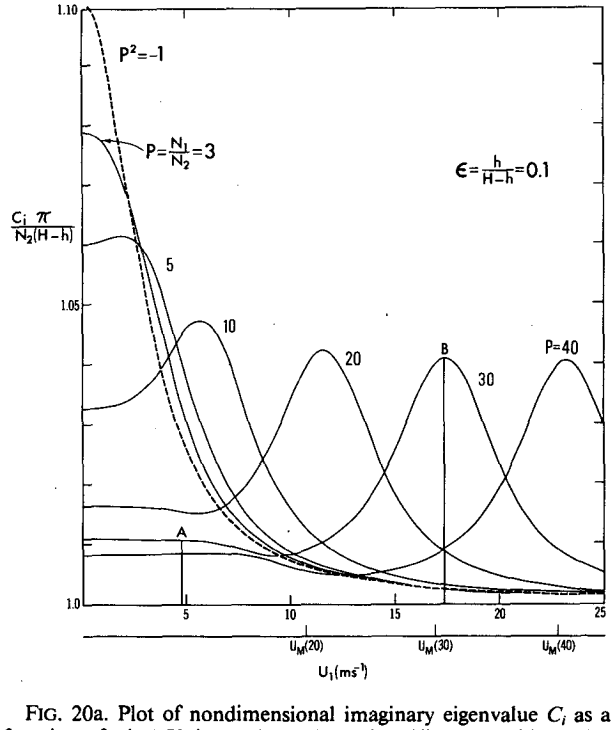

FIG. 20a. Plot of nondimensional imaginary eigenvalue C_i as a function of wind U_1 in the lower layer for different stability ratios P. Supplementary axis at bottom indicates dimensional values of U_{1M} as calculated from (4.15) for the values of P given in the brackets.

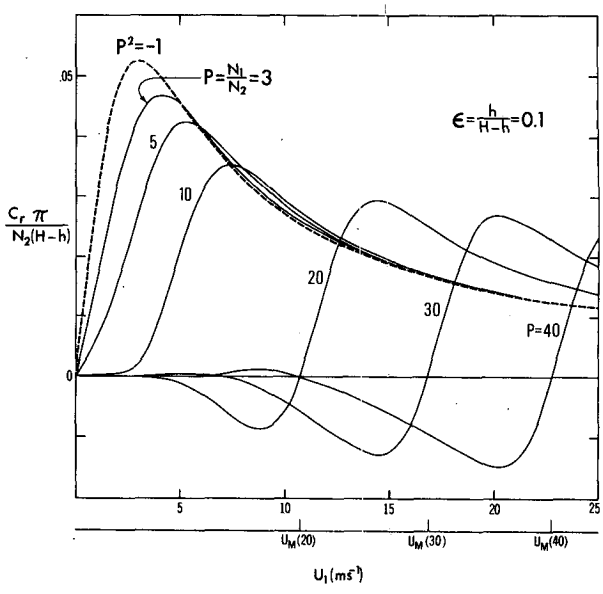

FIG. 20b. As in Fig. 20a but for nondimensional real eigenvalue C_r.

Equation (4.10) may be expressed in terms of its real and imaginary parts as follows:

$$\frac{P\sinh 2\gamma_{2r}(H-h)}{\cosh 2\gamma_{2r}(H-h)+\cos 2\gamma_{2i}(H-h)} = -\frac{\sin 2\gamma_{1r}h}{\cos 2\gamma_{1r}h+\cosh 2\gamma_{1i}h}, \quad (4.11a)$$

$$\frac{P\sin 2\gamma_{2i}(H-h)}{\cosh 2\gamma_{2r}(H-h)+\cos 2\gamma_{2i}(H-h)} = -\frac{\sinh 2\gamma_{1i}h}{\cos 2\gamma_{1r}h+\cosh 2\gamma_{1i}h}. \quad (4.11b)$$

As Fig. 20b shows, the phase speed c_r is small for any value of U_1. Also, an important feature is that c_r is nearly equal to zero for values of U_1 corresponding to the peak growth rate (Fig. 20a). We will now consider these points in more detail.

When $c_r = 0$, then $\gamma_{2r} = 0$ so (4.11a) and (4.11b) reduce to

$$2\gamma_{1r}h = n\pi, \tag{4.12a}$$

$$\frac{P\sin 2\gamma_{2i}(H-h)}{1+\cos 2\gamma_{2i}(H-h)} = -\frac{\sinh 2\gamma_{1i}h}{\cosh 2\gamma_{1i}h + (-1)^n}, \tag{4.12b}$$

where $n = 1, 2, \ldots$. Because c_r is small in the present case, we may use the following approximations to (4.9a) and (4.9b):

$$\gamma_{1r} \approx \frac{N_1 U_1}{U_1^2 + c_i^2}, \quad \gamma_{1i} \approx \frac{c_i N_1}{U_1^2 + c_i^2}, \tag{4.13a}$$

$$\gamma_{2r} \approx 0, \qquad \gamma_{2i} \approx -N_2/c_i. \tag{4.13b}$$

Then (4.12a) states that

$$\frac{N_1 U_1}{U_1^2 + c_i^2} h = \frac{n\pi}{2},$$

so we may solve for the value U_{1M} for which c_i is maximum to obtain

$$U_{1M} = \frac{N_1 h}{n\pi} \pm \left[\left(\frac{N_1 h}{n\pi}\right)^2 - c_i^2\right]^{1/2}.$$

This equation may be normalized by $N_2(H-h)\pi^{-1}$ to give

$$\mathcal{U}_{1M} = \frac{U_1 \pi}{N_2(H-h)} = \frac{P\epsilon}{n} \pm \left[\left(\frac{P\epsilon}{n}\right)^2 - C_i^2\right]^{1/2}. \tag{4.14}$$

For $n = 1$ with $C_i^2 = 1$,

$$\mathcal{U}_{1M} = P\epsilon \pm [(P\epsilon)^2 - 1]^{1/2}. \tag{4.15}$$

Calculated values of U_{1M} are marked along the abscissa of Fig. 20 and coincide, as expected, with the maxima of c_i so long as $P\epsilon > 1$ (since $\epsilon = 0.10$, this implies that $P > 10$ in order for the mode $n = 1$ to occur). The quantity $\mathcal{U}_{1M}$ in (4.15) can be interpreted as the normalized wind speed required to sustain a standing gravity wave of vertical wavenumber 1 in the stably stratified lower layer. Higher vertical wavenumber modes ($n = 2, 3\cdots$) can be generated for lower wind speeds. It can also be seen from (4.12) and (4.14) that the peak value $c_{i_{\max}}$ becomes independent of N_1 for $U_1^2 \gg c_{i_{\max}}^2$ (as seen for the curves for which $P > 10 = \epsilon^{-1}$ in Fig. 20a) with a value

$$\mathcal{U}_{1M} \approx 2P\epsilon$$

when $P\epsilon \gg 1$, or in dimensional form:

$$U_{1M} = 2N_1 h/\pi. \tag{4.16}$$

For $n = 1$, (4.12b) may be written as

$$\left[\sin\left(2\frac{N_2}{c_i}(H-h)\right)\right]\left[1+\cos\left(\frac{2N_2}{c_i}(H-h)\right)\right]^{-1} = \frac{1}{P}\left[\sinh\left(2\frac{c_i N_1}{U_{1M}^2 + c_i^2}h\right)\right] \times \left[\cosh\left(2\frac{c_i N_1}{U_{1M}^2 + c_i^2}h\right) - 1\right]^{-1}.$$

Under the assumption $c_i \ll U_{1M}$, the right-hand side may be simplified by expanding the numerator and denominator in Taylor expansions. Then by using (4.16), we obtain finally

$$\sin\left(2\frac{N_2}{c_i}(H-h)\right)\left[1+\cos\left(2\frac{N_2}{c_i}(H-h)\right)\right]^{-1} = \frac{N_2}{N_1}\frac{U_{1M}^2}{c_i N_1 h} = \frac{4}{\pi^2}\frac{N_2 h}{c_i}. \tag{4.17}$$

Note that (4.17) is independent of N_1. Thus the maximum value of c_i will be a constant for $P \gg \epsilon^{-1}$.

b. Structure of the unstable mode

Our primary reason for developing the two-layer model is to produce examples of the different configurations of vertical motion which are possible in an environment in which a stable region with different wind intensities lies beneath a convectively unstable cloud layer. We will therefore concentrate in the remainder of this section upon two specific cases taken from the range of conditions shown in Fig. 20. These cases, indicated by the vertical lines labeled A and B in Fig. 20a, are the local instability maxima for the stability ratio $P = 30$ and are typical examples of weak ($U_1 = 4.75$ m s^{-1} for case A) and strong ($U_1 = 17.35$ m s^{-1} for case B) low-level winds.

The amplitude and phase of the eigenfunctions which correspond to these two cases are shown in Fig. 21. Note that the sinusoidal structure required for the single-layer case still predominates in the unstable upper layer of both eigenfunctions. However, in the stable layer, the curvature of the amplitudes and the value of the phases differ considerably.

In order to clarify the differences between these two eigenfunctions, the two-dimensional fields of the normalized vertical motion and the normalized horizontal convergence over one wavelength are plotted in Figs. 22 and 23 for cases A and B, respectively. In comparing these two cases, it should be kept in mind that the low-wind case A with $U_1 = 4.75$ m s^{-1} is more representative of the wind differential between the cloud and subcloud layer, as occurred in the numerical solution described in Section 3 and the observed case of Ogura and Liou (1980). It is evident from a comparison of the convergence fields of Figs. 22 and 23 that the low-wind case predicts a phase shift of 180° between the convergence maximum at the level of free convection and the maximum at the surface. On the other hand, the convergence regions between these two levels remain in phase in the high-wind case B.

Hence the simple two-layer model predicts that, under certain wind conditions, a midlevel updraft will occur which is displaced from the associated low-level convergence. In fact, Fig. 22 shows divergence occurring beneath the midlevel convergence. While the configuration of midlevel convergence above low-level di-

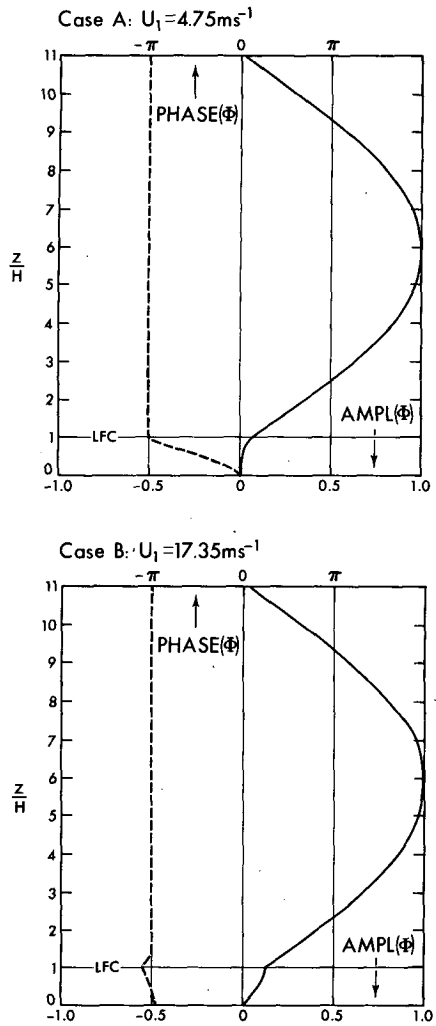

FIG. 21. Plots of the amplitude and phase of the complex eigensolution Φ of (4.5) with the stability ratio $P = 30$ for weak (A) and strong (B) low-level wind cases as indicated by the corresponding letters (and vertical lines) on the $P = 30$ curve of Fig. 20a.

vergence as shown in Fig. 22 is suggestive of the observed dual updraft structure, it would be difficult to predict from this simple model the actual phase shift which would occur between mid- and low-level convergence zones in an observed cloud system. The primary problem is the strong dependence of the growth rate curve, for fixed U_1, upon the stability ratio P (see Fig. 20). While N_1 may be determined easily, the stratification within the unstable convective layer, which would define N_2 and hence P, is difficult to determine. (The average vertical derivative of the equivalent potential temperature within the cloud zone above the LFC would seem to provide the most appropriate measure of this stratification.)

To summarize, we have attempted with this simple model to address two issues: 1) the sensitivity of the structure of the unstable gravity mode to the low-level wind, and 2) the location of the horizontal convergence zone inside the convective system. Concerning the first point, we have found that this system is weakly sensitive to low-level winds. (As Fig. 20 shows, the growth rate varies by 10% or less over the range of values of U_1.) This lack of sensitivity is due to the high gravitational instability of the configuration. Probably, with a CISK-type parameterization, an enhancement of this sensitivity would be found.

Concerning the second point, the most important feature of the model solutions shown in Figs. 22 and 23 is not the detailed convergence structure but rather the occurrence of intense convergence in the unstable layer immediately above the level of free convection. This result implies that a convergence maximum should occur in a moist convective system around the level of free convection. Such a result is physically reasonable since air parcels rising within the cloud

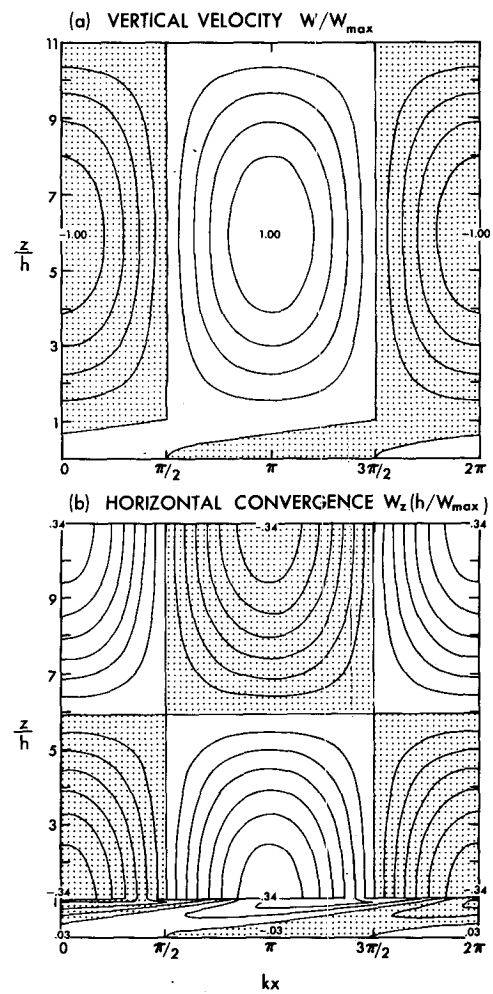

FIG. 22. Contour plots, over one wavelength, of the distribution of normalized vertical velocity and horizontal convergence associated with the weak low-level wind eigenfunction A (U_1 = 4.75 m s^{-1}) of Fig. 21.

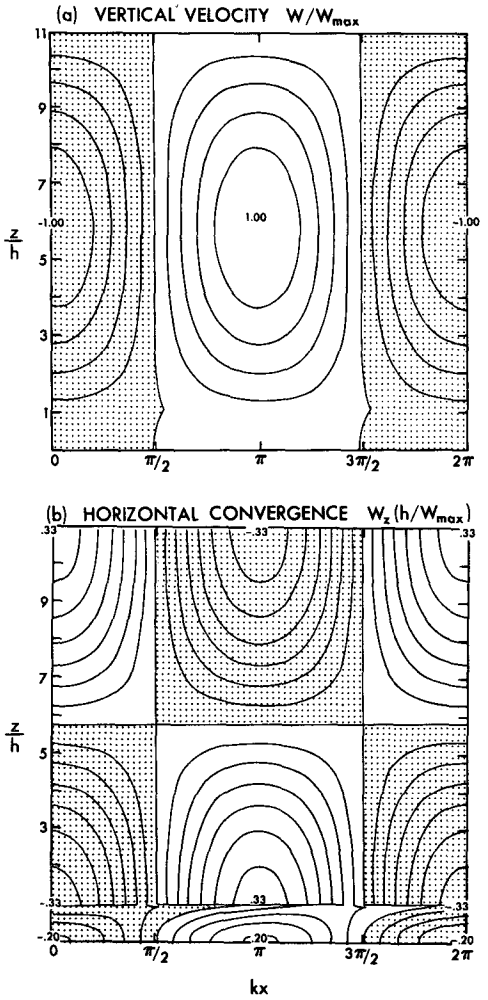

FIG. 23. As in Fig. 22, but for the eigenfunction B corresponding to strong low-level wind U_1 = 17.35 m s^{-1} as shown in Fig. 21.

updraft will first encounter a net positive buoyancy upon reaching this level. Hence the presence of a convergence maximum at midlevels, as found in the observed and simulated cases, may be a universal feature of convectively unstable cloud systems, occurring in that region of the cloud which is driven most intensely by a net positive buoyancy due to latent heat release. The second updraft, which occurs in the stable air below the cloud zone, may occur as forced convection, as in the moist front simulation described in Section 3, with its position relative to the midlevel updraft determined by the stability ratio N_1/N_2, the stable layer depth, and the wind differential between the stable and unstable layers.

5. Discussion and summary

An analysis has been made of the mesoscale structure of the front and convective system in the numerical simulation of an observed frontal system described by Ross and Orlanski (1982). This analysis focuses on 1) the evolution of the surface kinematics and dynamics within the frontal zone and 2) the development and structure of the moist convection which occurs within the frontal system. The model used to produce the solutions (see RO for details) uses an explicit representation of convection and assumes no surface drag.

Analysis of the surface distribution of vertical vorticity and horizontal convergence reveals a progressive evolution of the frontal system through three phases: frontogenetic growth, mature quasi-steady state, and frontolytic decay. Initially, the frontal vorticity pattern sharpens and intensifies, due in part to an adjustment of the front from meso-α scale initial conditions to the meso-β scale dynamics of the 61.5 km grid model. During this initial period, the vorticity and convergence zones are in alignment, thus producing strong vortex stretching. However, at 12 h the convergence maximum has moved well ahead of the vorticity, thereby causing a greatly reduced vorticity growth. The front then evolves into a mature, quasi-steady system during a middle period from 24 to 36 h which is characterized by approximately constant surface vorticity and convergence which appear to oscillate about an equilibrium state. Finally, from 42 to 48 h frontolysis dominates as the magnitudes of both vorticity and convergence decrease considerably.

An analysis of the prognostic equations for surface vorticity and divergence reveals that ageostrophic effects, which develop in the divergence equation as vorticity intensifies, tend to produce the observed shift of the convergence peak ahead of the vorticity. This ageostrophic effect thus represents a negative feedback mechanism, because the displacement of convergence, as vorticity intensifies, tends to inhibit further vortex stretching. It is important to note that this feedback mechanism acts to prevent the larger frontogenetic growth which would occur if vorticity and divergence were in phase. Also, it should be recognized that any system of equations which is to properly represent this effect must include a prognostic prediction of divergence tendencies so that departures from geostrophy produce changes in divergence. Quasi-geostrophic equations, which predict divergence diagnostically from the potential temperature equations, are thus not able to represent this phase shift effect.

The above feedback mechanism represents a frontolytic process which acts to inhibit frontogenetic growth in developing fronts and to determine the scale of the cyclonic vorticity band within the mature steady-state front. As vorticity develops in the frontogenetic phase, feedback in the form of the ageostrophic term $f(\zeta - \zeta_g)$ in the divergence equation (2.6) will tend to reduce convergence, thereby producing a phase shift between vorticity and divergence. As a result, the stretching of vorticity will be limited to the region of the frontal zone where convergence overlaps cyclonic

vorticity. In order for the front to achieve a steady-state condition, this frontogenetic stretching of the relative vorticity, together with the Coriolis stretching term $f\mathcal{D}$, must be balanced by viscous dissipation. However, the width of the band of cyclonic vorticity in this steady-state front will be determined by the feedback mechanism rather than by the amount of viscous dissipation.

The insensitivity of the width of the cyclonic vorticity band to viscosity was demonstrated in the comparison study discussed in Section 2a and summarized by Fig. 4. As this study showed, the magnitude of the maximum cyclonic vorticity increased as the viscosity near the surface was reduced, but the width of the cyclonic vorticity band remained unchanged. The study of Williams (1974) on the sensitivity of steady-state two-dimensional fronts to different horizontal and vertical viscosity coefficients is relevant to the present case (although Williams assumed a no-slip condition at the surface compared to the free-slip condition used here). Using his definition of the frontal scale in terms of the horizontal temperature field, we find a scale of roughly 380 km for the present dry control solution at 36 h. This is in reasonable agreement with Williams' result if the low-level vertical viscosity of 20 $m^2 s^{-1}$ is assumed to be controlling in the present case. (The horizontal viscosity of 10^4 $m^2 s^{-1}$ in all cases presented here implies a frontal scale, in Williams' terms, of approximately 100 km and does not appear to be a controlling factor in the solution.) When the vertical viscosity was reduced to 5 $m^2 s^{-1}$ (lowest frames of Fig. 4), the horizontal scale of the temperature field was reduced to 280 km as a result of the increased thermal wind shear permitted by the lower vertical viscosity value. This reduced scale is also consistent with Williams' results (see his Fig. 8). However, our Fig. 4 shows that the scale of the cyclonic vorticity band remains constant at approximately 220 km in both cases. Hence the vorticity band width, as a measure of the dynamic scale of the frontal zone, is unchanged by the viscosity differences.

The frontal configuration in which divergence is ahead of and out of phase with vorticity near the surface is one which is quite justifiable in terms of a simple streamline analysis. Figure 24 shows a schematic representation of streamlines within such a surface front and is similar to the 30 h pattern shown in Fig. 1. It also bears a strong resemblance to the pattern on an isentropic surface within a frontal zone as shown schematically by Green *et al.* (1966). In a coordinate system oriented so that y is along the front and x is across the front, the long-front velocity component v changes sign where vorticity (approximately v_x) is maximum. Maximum convergence then occurs ahead of the vorticity maximum in a region where the cross-front wind component u changes sign and the vorticity is approximately zero. Hence, parcels on the warm air side of the front will be drawn into the convergence zone without experiencing any cyclonic turning. On the other hand, parcels entering the frontal zone from the cold air side will undergo a strong cyclonic turning, with the long-front wind component changing sign, before being lifted within the convergence zone.

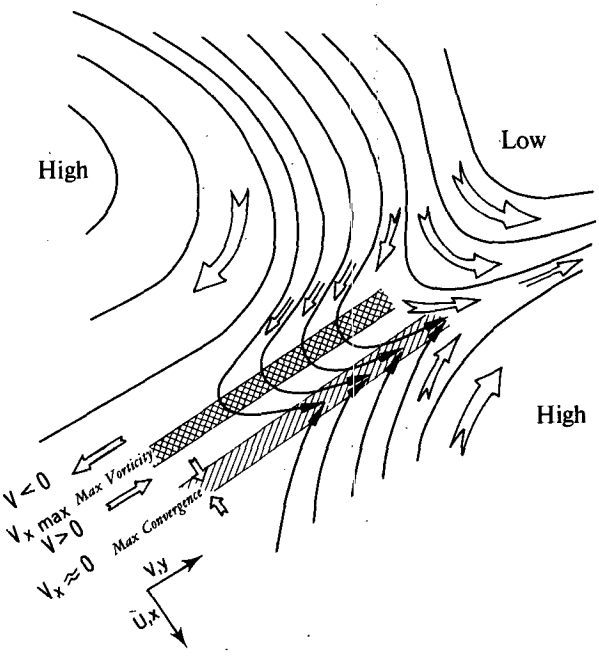

FIG. 24. Sketch of proposed streamline pattern near the surface within a cold frontal zone with the cold air mass at the top of the figure. A coordinate system relative to the front is shown where x is the cross-front coordinate and y is the long-front coordinate. The line of maximum vorticity (v_x maximum) is indicated by cross-hatching. The line of maximum convergence is shown by hatching. Vorticity v_x will be zero along the maximum convergence line if vorticity and convergence are 90° out of phase.

Evidence from reported observations of frontal circulations fails to either prove or disprove the existence of a phase shift in observed mature frontal systems, due largely to the coarseness of the observing networks used in these studies. The observed front analyzed by Ogura and Portis (1982) is a case with a similar although somewhat smaller scale to the front considered here. The vertical cross-sections of vertical vorticity and vertical p-velocity ω presented in their paper (their Figs. 18 and 19, respectively) suggest a possible phase shift between vorticity and convergence at the surface, but the horizontal maps of these fields (their Figs. 8 and 9, respectively) do not support this. Unfortunately, the ratiosonde spacing of roughly 250 km in the SESAME field experiment, from which their data-set was taken, is still inadequate to make a definitive statement regarding this. Future field programs which employ remote sensing systems such as wind profilers and Doppler radars may provide observations with sufficient accuracy to clarify this issue.

When moisture was included in the model, the frontal solution was found to be essentially unchanged

from its dry counterpart until unstable convection developed at around 24 h. At this time, the increased lifting due to the convection first intensified the vorticity by vortex stretching. The surface vorticity and convergence patterns, which formed two-dimensional bands in the dry case, began to break up into cells similar in structure to the frontal rainband precipitation patterns observed by Hobbs and Biswas (1979). Indications are that the breakdown of the banded structure into cells is a manifestation of a conditional barotropic instability triggered by the intensifying frontal vorticity.

The squall line which forms along the front develops in stages. Initially condensation occurs above the nose of the front as frontal lifting raises moist air from the warm sector as forced convection. Then, at 24 h a condition of free convection is achieved more to the rear of the system, leading to deep convection which penetrates above the tropopause. The resulting mature squall line exhibits a strong convergence maximum at around 3 km with a weaker convergence zone occurring near the surface at the nose of the front.

In the Appendix, terms are displayed for each of the prognostic equations from the moist solution at 36 h in a vertical plane oriented perpendicular to the surface front and passing through the region of intense convection within the squall line. In particular, the terms for potential temperature show a very close balance between adiabatic cooling and diabatic heating within the cloud zone. As a result the major heating within the convective system occurs as adiabatic warming in the region of subsidence in the clear air to the rear of the cloud. An analogous balance was also found between upward advection and condensation of water vapor within the cloud zone. Both results demonstrate that the explicit representation of convection used by the model is able to produce physically reasonable results even though the model resolution is clearly too coarse to resolve individual convective elements of the actual squall line.

An analysis was made of the dual updraft structure of the simulated squall line in an effort to determine the mechanisms which produce it. At first sight, this pattern suggests merely the finite difference representation of upgliding advection along the frontal isentropes. However, Ogura and Liou (1980) observed a strikingly similar double updraft in their analysis of an Oklahoma squall line not associated with a front. This similarity implies that the updraft structure is associated with the convective system rather than the cold front.

Ogura and Liou suggested that the formation of the midlevel convergence zone above a divergence zone near the surface occurs because waterloading and rainwater evaporation produce divergence beneath the cloud. However, the present model, with its similar updraft structure, does not have a rainwater phase. Therefore, only the weak cooling effect of the evaporation of cloudwater could be used to explain the divergence zone.

An alternative hypothesis has been proposed to explain this structure. Specifically, the formation of the midlevel convergence out of phase with the low-level convergence is assumed to be a manifestation of one of the modes which develops from the convectively unstable cloud/subcloud environment. To test this hypothesis, a simple dry model has been formulated which consists of a stably-stratified lower layer beneath an unstably-stratified upper layer. Different but uniform winds are assumed to exist within the upper and lower layers to represent different wind conditions in the cloud and subcloud layers.

For certain wind and stability conditions, the resulting eigenfunctions which are produced by this simple model do show the desired phase shift between the convergence maximum just above the interface and the maximum near the surface. For stability conditions typical of the cloud–subcloud environment, a 180° phase shift was found to occur for weak low-level winds, while the maximum were in phase when low-level winds were strong.

These features of the unstable modes indicate a possible explanation for the dual updraft structure. However, a more fundamental and universal result from the model is the finding that a convergence maximum occurs immediately above the interface between the stable and unstable layers for all wind conditions. To the extent that the simple dry model reflects the behavior of the cloud environment, this result suggests that a convergence maximum should occur immediately above the level of free convection within the convectively unstable cloud. This is physically reasonable since air parcels should undergo a strong acceleration upon encountering the positive buoyancy at and above this level.

Acknowledgments. The authors would like to thank the referees, especially Drs. Terry Williams and Dan Keyser, for their assistance in helping to clarify and improve the manuscript. We are also most grateful to Messrs. Rich Shaginaw and Larry Polinsky for their programming assistance. We thank Dr. Ian Simmonds for providing the spline interpolation subroutine and the NCAR computing staff for providing the graphical map data of North America which are used in the figures. Finally, we appreciate the patience and skill exhibited by Mmes. Betty Williams and Joyce Kennedy in typing the manuscript and by Messrs. John Connor, Phil Tunison and other members of the GFDL Graphics Support Staff in preparing the figures.

APPENDIX

Terms from the Moist Solution

In order to indicate the dynamic and thermodynamic balances which exist in the simulated moist

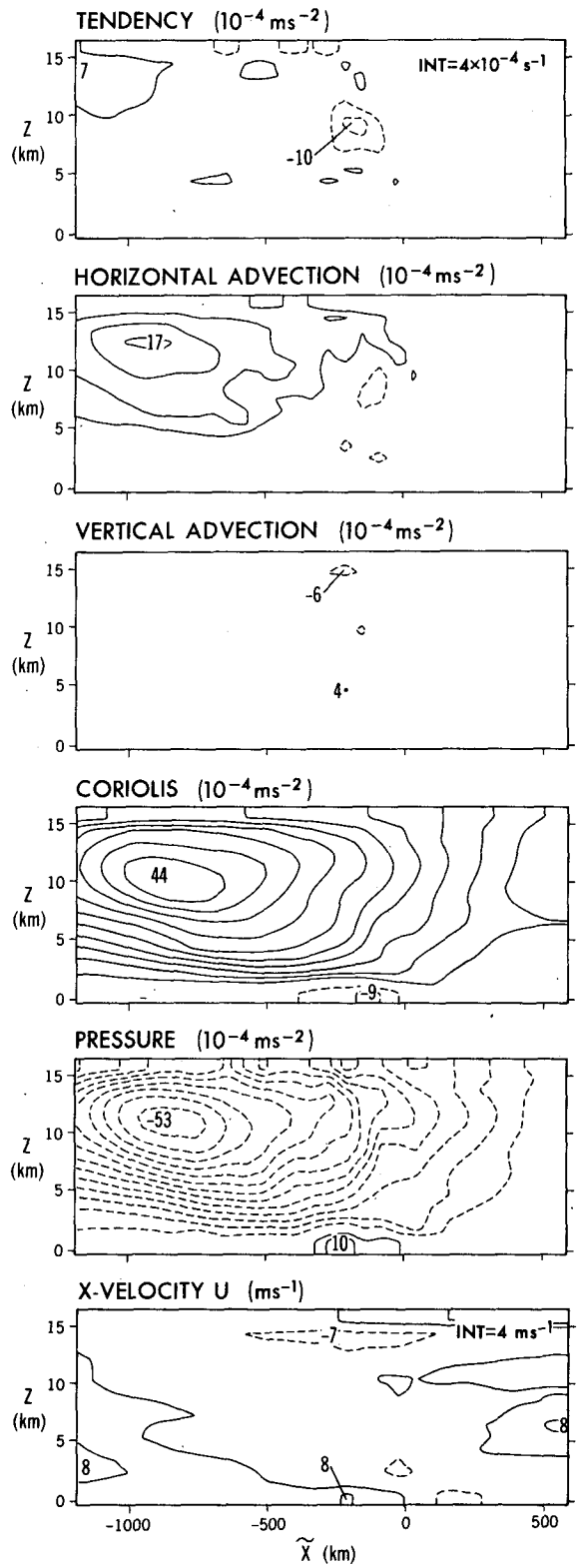

FIG. 25. Distribution of terms of the x-momentum equation (divided by density ρ_0) from the moist solution at 36 h in the vertical cross-section (aligned with line PQ of Fig. 6b), as in Fig. 12. The basic field itself is shown in the lowest frame. The horizontal distance $\tilde{x}$ along the cross-section is adjusted so that the origin is located at the surface maximum of vertical vorticity within the front. Distance $\tilde{x}$ increases from cold to warm air (i.e., from P to Q). The contour intervals INT for the terms are shown in the upper frame and for the basic field in the lower frame. The stress term, not shown, has a maximum of 3×10^{-4} m s^{-2} located at $(\tilde{x}, z) = (-246, 14.5)$ km and a minimum of -2×10^{-4} m s^{-2} at $(-61, 8.5)$ km.

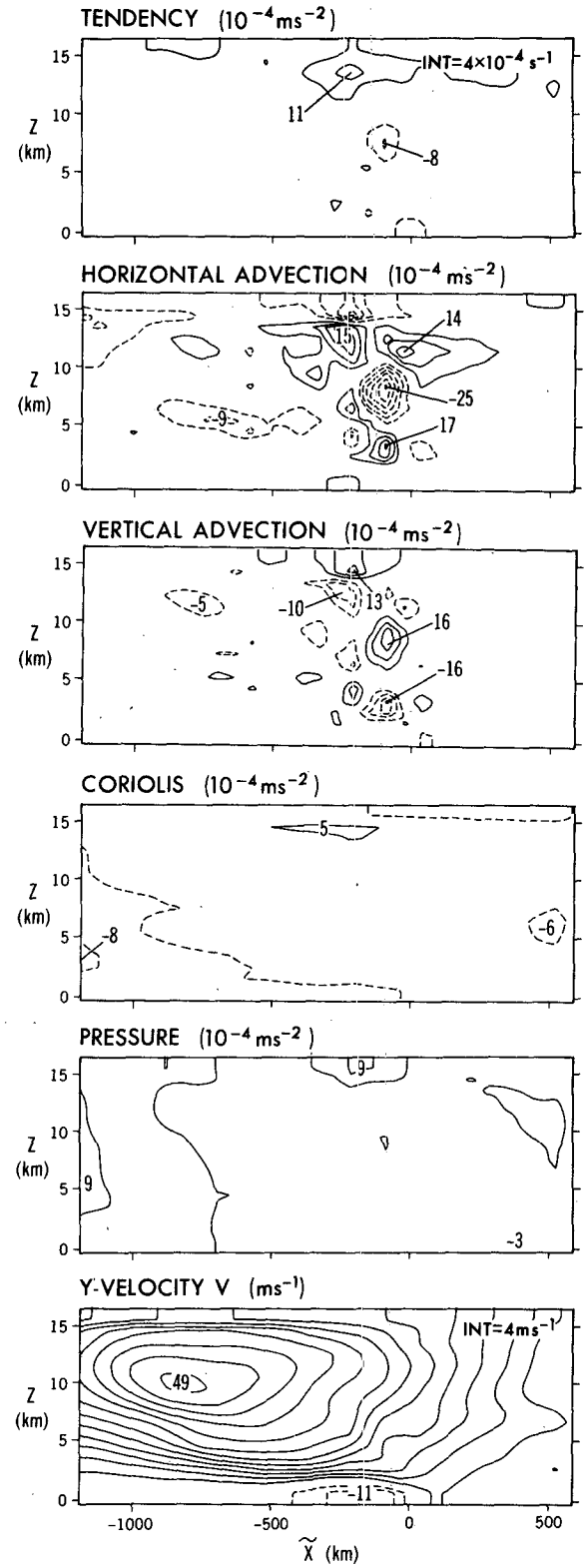

FIG. 26. As in Fig. 25, but for y-momentum (divided by density ρ_0). The stress term, not shown, has a maximum of 3×10^{-4} m s^{-2} located at $(\tilde{x}, z) = (-61, 0.5)$ km and a minimum of -2×10^{-4} m s^{-2} at $(-184, 3.5)$ km.

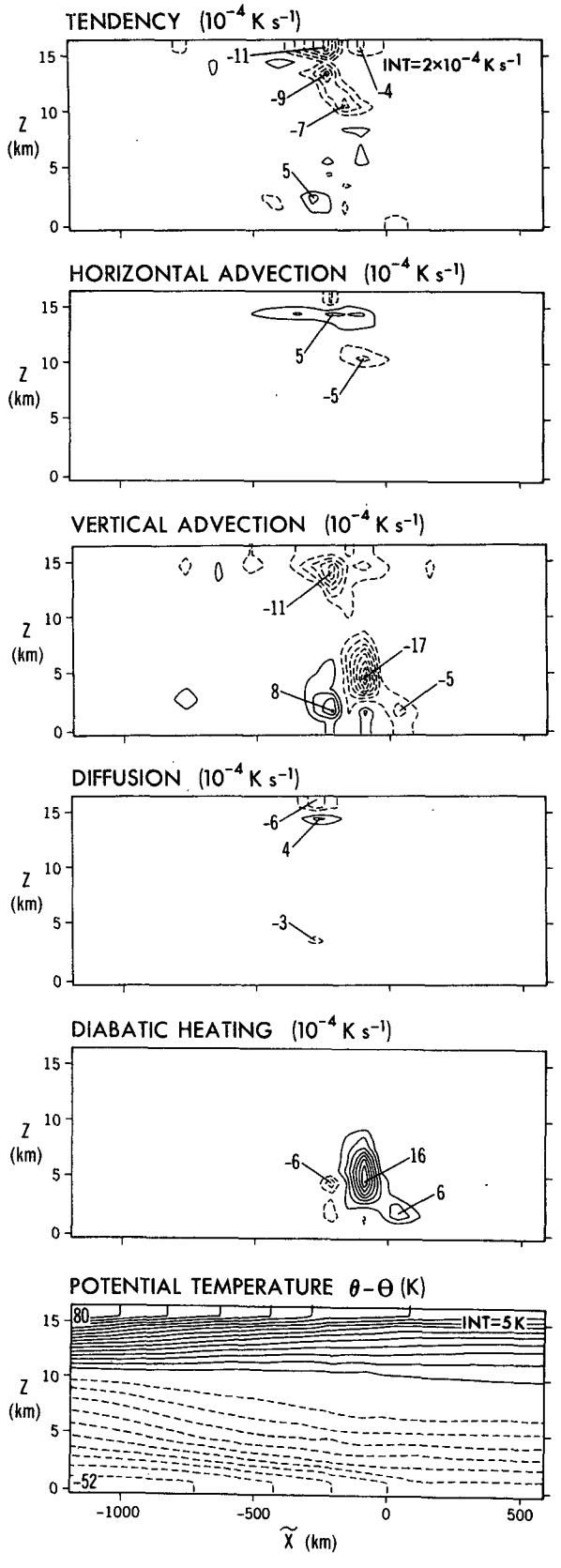

FIG. 27. As in Fig. 25, but for potential temperature. The reference temperature Θ is 328 K.

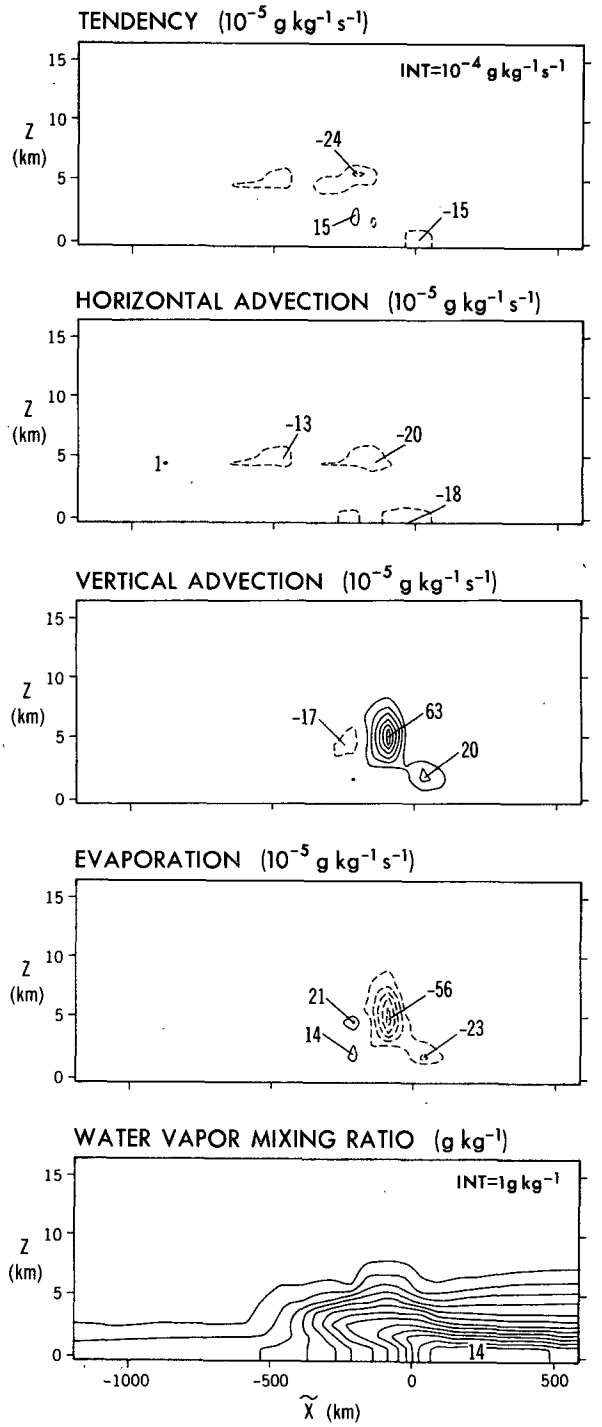

FIG. 28. As in Fig. 25, but for water vapor mixing ratio. The diffusion term, not shown, has a maximum of 9×10^{-5} g kg^{-1} s^{-1} located at $(\tilde{x}, z) = (553, 0.5)$ km and a minimum of -10×10^{-5} g kg^{-1} s^{-1} at (62, 0.5) km.

front, we display here the distribution of the terms in the equations of motion from the moist numerical solution at 36 h. Important terms are shown for each of the five tendency equations, namely: x-momentum

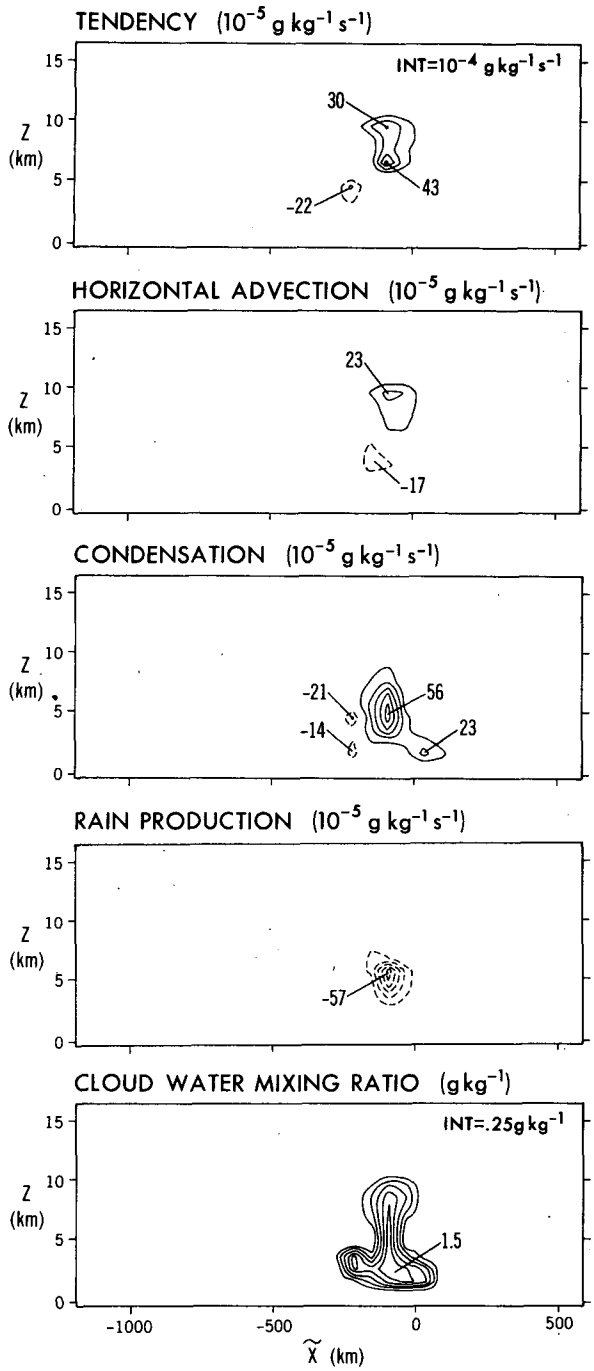

FIG. 29. As in Fig. 25, but for cloudwater mixing ratio. The vertical advection term, not shown, has a maximum of 7×10^{-5} g kg^{-1} s^{-1} located at $(\tilde{x}, z) = (-184, 1.5)$ km and a minimum of -5×10^{-5} g kg^{-1} s^{-1} at (62, 0.5) km. The diffusion term, also not shown, has a maximum of 4×10^{-5} g kg^{-1} s^{-1} at $(\tilde{x}, z) = (0, 0.5)$ km and a minimum of -8×10^{-5} g kg^{-1} s^{-1} at (184, 3.5) km.

$\rho_0 u$, y-momentum $\rho_0 v$, potential temperature θ, water vapor mixing ratio q and cloudwater mixing ratio c. These quantities are then interpolated to a vertical x–z grid which is oriented perpendicular to the surface front along the line PQ in Fig. 6. The x- and y-advection terms are combined to form a term for horizontal advection. Also, the momentum equations, which represent components aligned with the model Cartesian coordinates x and y, are rotated by a coordinate transformation to form equations for $\rho_0 \tilde{u}$ and $\rho_0 \tilde{v}$ which are the respective horizontal momentum components within the plane and perpendicular to the plane $\tilde{x}$–$\tilde{z}$ of the rotated cross-section. These momentum terms are divided by density ρ_0 so that the terms approximate the tendency equations for u and v. The resulting fields for each of the terms are plotted in Figs. 25–29. Note that terms (primarily viscous) are not plotted in the figures when their maximum values are less than the first contour interval of the plot (although the maximum and minimum values are given in the captions). Plots of each of the basic quantities, $\rho_0 \tilde{u}$, $\rho_0 \tilde{v}$, θ, q and c, at 36 h, are presented at the bottom of each figure showing the terms for the corresponding tendency equation. The tendency term in each figure is the sum of all other terms in the equation.

REFERENCES

Andrews, D. G., and B. J. Hoskins, 1978: Energy spectra predicted by semi-geostrophic theories of frontogenesis. *J. Atmos. Sci.*, **35**, 509–512.

Blumen, W., 1980: A comparison between the Hoskins–Bretherton model of frontogenesis and the analysis of an intense surface frontal zone. *J. Atmos. Sci.*, **37**, 64–77.

Cerasoli, C. P., 1979: Experiments on buoyant-parcel motion and the generation of internal gravity waves. *J. Fluid Mech.*, **86**, 247–271.

Charney, J. G., 1971: Geostrophic turbulence. *J. Atmos. Sci.*, **28**, 1087–1095.

Emanuel, K. A., 1982: Inertial instability and mesoscale convective systems. Part II: Symmetric CISK in a baroclinic flow. *J. Atmos. Sci.*, **39**, 1080–1097.

Green, J. S. A., F. H. Ludlam and J. F. R. McIlveen, 1966: Isentropic relative-flow analysis and the parcel theory. *Quart. J. Roy. Meteor. Soc.*, **92**, 210–219.

Hamming, R., 1962: *Numerical Methods for Scientists and Engineers.* McGraw-Hill, 411 pp.

Hobbs, P. V., 1978: Organization and structure of clouds and precipitation on the mesoscale and microscale in cyclonic storms. *Rev. Geophys. Space Phys.*, **16**, 741–755.

——, and K. R. Biswas, 1979: The cellular structure of narrow cold-frontal rainbands. *Quart. J. Roy. Meteor. Soc.*, **105**, 723–727.

Hoskins, B. J., 1976: Baroclinic waves and frontogenesis: introduction and Eady waves. *Quart. J. Roy. Meteor. Soc.*, **102**, 103–122.

——, and F. P. Bretherton, 1972: Atmospheric frontogenesis models: Mathematical formulation and solution. *J. Atmos. Sci.*, **29**, 11–37.

——, and N. V. West, 1979: Baroclinic waves and frontogenesis. Part II: Uniform potential vorticity jet flows—cold and warm fronts. *J. Atmos. Sci.*, **36**, 1663–1680.

James, P. K., and K. A. Browning, 1979: Mesoscale structure of line convection at surface cold fronts. *Quart. J. Roy. Meteor. Soc.*, **105**, 371–382.

Keyser, D., and R. A. Anthes, 1982: The influence of the planetary boundary layer physics on frontal structure in the Hoskins–Bretherton horizontal shear model. *J. Atmos. Sci.*, **39**, 1783–1802.

Kuo, H. L., 1963: Perturbations of a plane Couette flow in stratified fluid and origin of cloud streets. *Phys. Fluids,* **6,** 195–211.

McWilliams, J. C., and P. R. Gent, 1980: Intermediate models of planetary circulations in the atmosphere and ocean. *J. Atmos. Sci.,* **37,** 1667–1678.

Mechoso, C. R., 1980: The atmospheric circulation around Antarctica: Linear stability and finite-amplitude interactions with migrating cyclones. *J. Atmos. Sci.,* **37,** 2209–2233.

Moore, G. W. K., 1983: On the structure of the narrow cold-frontal rainband. Ph.D. dissertation, Princeton University, 141 pp.

Ogura, Y., and M. T. Liou, 1980: The structure of a midlatitude squall line: A case study. *J. Atmos. Sci.,* **37,** 553–567.

——, and D. Portis, 1982: Structure of the cold front observed in SESAME-AVE III and its comparison with the Hoskins–Bretherton frontogenesis model. *J. Atmos. Sci.,* **39,** 2773–2792.

Orlanski, I., 1981: The quasi-hydrostatic approximation. *J. Atmos. Sci.,* **38,** 572–582.

——, and B. B. Ross, 1977: The circulation associated with a cold front. Part I: Dry case. *J. Atmos. Sci.,* **34,** 1619–1633.

Rosenthal, S. L., 1979: The sensitivity of simulated hurricane development to cumulus parameterization details. *Mon. Wea. Rev.,* **107,** 193–197.

Ross, B. B., and I. Orlanski, 1982: The evolution of an observed cold front. Part I: Numerical simulation. *J. Atmos. Sci.,* **39,** 296–327.

Williams, R. T., 1967: Atmospheric frontogenesis: A numerical experiment. *J. Atmos. Sci.,* **24,** 627–641.

——, 1974: Numerical simulation of steady state fronts. *J. Atmos. Sci.,* **31,** 1286–1296.

——, and J. Plotkin, 1968: Quasi-geostrophic frontogenesis. *J. Atmos. Sci.,* **25,** 201–206.